Journal of Structural Geology 33 (2011) 362–380

Contents lists available at ScienceDirect

Journal of Structural Geology

journal homepage: www.elsevier.com/locate/jsg

Structural and geochronological evidence for Early Cretaceous orogen-parallel extension of the ductile lithosphere in the northern Dabie orogenic belt, East China

Yongsheng Wang [a,*], Biwei Xiang [b], Guang Zhu [a], Dazhi Jiang [c]

[a] School of Resource and Environmental Engineering, Hefei University of Technology, Hefei, 230009, PR China
[b] Faculty of Earth Sciences, China University of Geosciences, Wuhan, 430074, PR China
[c] Department of Earth Sciences, University of Western Ontario, London, Ontario, N6A5B7, Canada

ARTICLE INFO

Article history:
Received 13 April 2010
Received in revised form
11 August 2010
Accepted 5 September 2010
Available online 16 September 2010

Keywords:
Dabie orogenic belt
North Dabie dome
Xiaotian-Mozitan shear zone
Wuhe-Shuihou shear zone
$^{40}Ar-^{39}Ar$ dating
orogen-parallel extension

ABSTRACT

The WNW-trending North Dabie dome (NDD) in the northern Dabie orogenic belt is bounded by the Xiaotian-Mozitan ductile shear zone (XMSZ) in the north and the Wuhe-Shuihou shear zone (WSSZ) in the south. Fabric geometries and kinematics of both the XMSZ and the WSSZ are similar. They both show a top-to-NW or WNW sense of shear and display similar microstructures which indicate that the deformation temperature was about 600–650 °C. $^{40}Ar-^{39}Ar$ dating of hornblende and biotite from the mylonites of the XMSZ suggests that the shear zone was developed prior to 142 Ma. U–Pb zircon LA-ICPMS dating of undeformed granite dikes that cut the XMSZ suggests that the ductile shearing occurred before 130 Ma. The WSSZ was also developed in the Early Cretaceous. The interior of the NDD is dominated by top-to-NW or WNW sense of shear in the migmatitic gneiss and deformed plutons of the earliest Early Cretaceous ages. We suggest that the XMSZ, the WSSZ, and the interior of the NDD were involved in the same Early Cretaceous deformation. The XMSZ and the WSSZ were originally a single connected, more flat-lying zone, which we call the East Dabie Detachment Zone (EDDZ). It developed at a crustal level of over 18 km in depth. Kinematics of the EDDZ suggest that the ductile crust and possibly part of the lithospheric mantle in the eastern Dabie orogen underwent pervasive orogen-parallel and ESE-ward extension at the beginning of the Early Cretaceous. Large-scale magmatic intrusions following this deformation and the resultant increase in buoyancy led to the exhumation of the NDD and the warping of the EDDZ. Erosion separated the EDDZ into two zones (the XMSZ and the WSSZ) as observed today. Many metamorphic core complexes of Early Cretaceous were developed in the eastern North China Craton, most showing top-to-NW or WNW sense of shear. We suggest that such a widespread uniform shear sense reflects a uniform flow direction of the ductile lithosphere in the East China that has also been documented in the Liaonan, Yiwulushan and Yumenshan metamorphic core complexes in the northeastern part of the North China Craton.

© 2010 Elsevier Ltd. All rights reserved.

1. Introduction

The Dabie orogenic belt (DOB) was developed by continent–continent collision between the North China Block (NCB) and the South China Block (SCB). Coesite-bearing (Okay et al., 1989; Wang et al., 1989) and microdiamond-bearing (Xu et al., 1992) eclogites from the ultra-high pressure (UHP) unit of the DOB suggest that part of the SCB crust was deeply subducted to mantle depth. In the past twenty years, detailed studies have shown that the collision took place in the Middle Triassic (ca. 240–230 Ma) (e.g., Ames et al., 1996; Rowley et al., 1997; Hacker et al., 2000; Li et al., 2000; Ayers et al., 2002) and the deeply subducted part of the SCB was exhumed to shallow crustal levels before Early Jurassic (e.g. Hacker et al., 2000; Li et al., 2005). Thereafter, the DOB is believed to have undergone lithosphere extension which leads to the formation of the North Dabie dome (NDD) (e.g. Zhong et al., 1998; Ratschbacher et al., 2000; Suo et al., 2001; Faure et al., 2003; Ma et al., 2004; Xie et al., 2006; Lin et al., 2007; Wang et al., 2007). However, the timing and nature of this extension remain controversial.

Structural evolution of the NDD is the key to understanding the lithosphere extension in the DOB. The NDD consists of migmatitic gneisses, Early Cretaceous plutons, and relics of UHP rocks which are bounded by the Xiaotian-Mozitan shear zone (XMSZ) in the

* Corresponding author.
E-mail address: yshw9007@126.com (Y. Wang).

0191-8141/$ – see front matter © 2010 Elsevier Ltd. All rights reserved.
doi:10.1016/j.jsg.2010.09.002

north and the Wuhe-Shuihou shear zone (WSSZ) in the south. Previous work showed that fabrics in the NDD indicate a top-to-NW or WNW sense of shear (Hacker et al., 2000; Faure et al., 2003; Lin et al., 2007). Many authors considered these fabrics to have developed during exhumation of the DOB in the Late Triassic to Early Jurassic (Hacker et al., 2000; Faure et al., 2003; Jiang et al., 2003a; Lin et al., 2007). Faure et al. (2003) and Lin et al. (2007) proposed that the NDD was a "syn-convergence" dome which was first developed during Late Triassic to Early Jurassic exhumation of the UHP slab and then was reworked by low-angle normal brittle faults in the Early Cretaceous. Zhong et al. (1998) and Suo et al. (2001) claimed that the NDD was a late-collisional gneiss dome with many radial shear zones and several detachment zones developed in the Middle Jurassic. Ratschbacher et al. (2000) argued that the NDD was a Cordillera-type, post-collisional metamorphic core complex which was developed in the Early Cretaceous by a rolling hinge-isostatic rebound model along the pre-existing XMSZ.

The timing and kinematics of the bounding shear zones, the XMSZ and the WSSZ, are also controversial. Proposals for the kinematics of the XMSZ include normal shear sense (e.g. Maruyama et al., 1994; Faure et al., 2003; Jiang et al., 2003a; Lin et al., 2005), normal shear sense with a sinistral component (e.g., Hacker et al., 2000; Ratschbacher et al., 2000), or sinistral shear (Wang et al., 2003). Wang et al. (2000), Suo et al. (2000), Zhang et al. (2002), and Liu et al. (2005a,b) regarded the XMSZ as being developed in the Middle Triassic, whereas others considered it to occur in the Early Cretaceous (e.g. Faure et al., 1999; Ratschbacher et al., 2000; Lin et al., 2005). No isotopic dating of mylonites has been reported from the XMSZ. Ratschbacher et al. (2000) obtained a $^{40}Ar-^{39}Ar$ biotite age of 120.5 Ma from a deformed gabbro near the XMSZ and interpreted it as the cooling age related to the development of the XMSZ. Zhong et al. (1998) and Suo et al. (2001) interpreted the WSSZ as a normal fault, whereas Hacker et al. (1995, 2000), Faure et al. (1999), Ratschbacher et al. (2000), and Jiang et al. (2003a) considered it as a thrust fault. The proposed ages for the WSSZ range from Middle Triassic (Zhang et al., 1996) to Early Cretaceous (Ratschbacher et al., 2000), or in between (Zhong et al., 1998; Suo et al., 2001).

In this contribution, we present detailed structural analysis of the XMSZ, the WSSZ, and the interior of the NDD. We also present geochronological data on the XMSZ. Our data place good constraints on the timing and kinematics of the deformation.

2. Geological setting

The DOB is truncated in the east by the NE-striking Tan-Lu fault zone (Fig. 1). To the west, it is separated from the Hong'an belt, the western part of the DOB, by the NE-striking Shang-Ma fault zone. To the south and north, the DOB is bounded by the Yangtze foreland fold and thrust belt and the Hefei Basin respectively. The Tan-Lu fault zone is a sinistral zone overprinted by a series of brittle normal faults (Zhu et al., 2005). The Shang-Ma fault zone is expressed by a series of

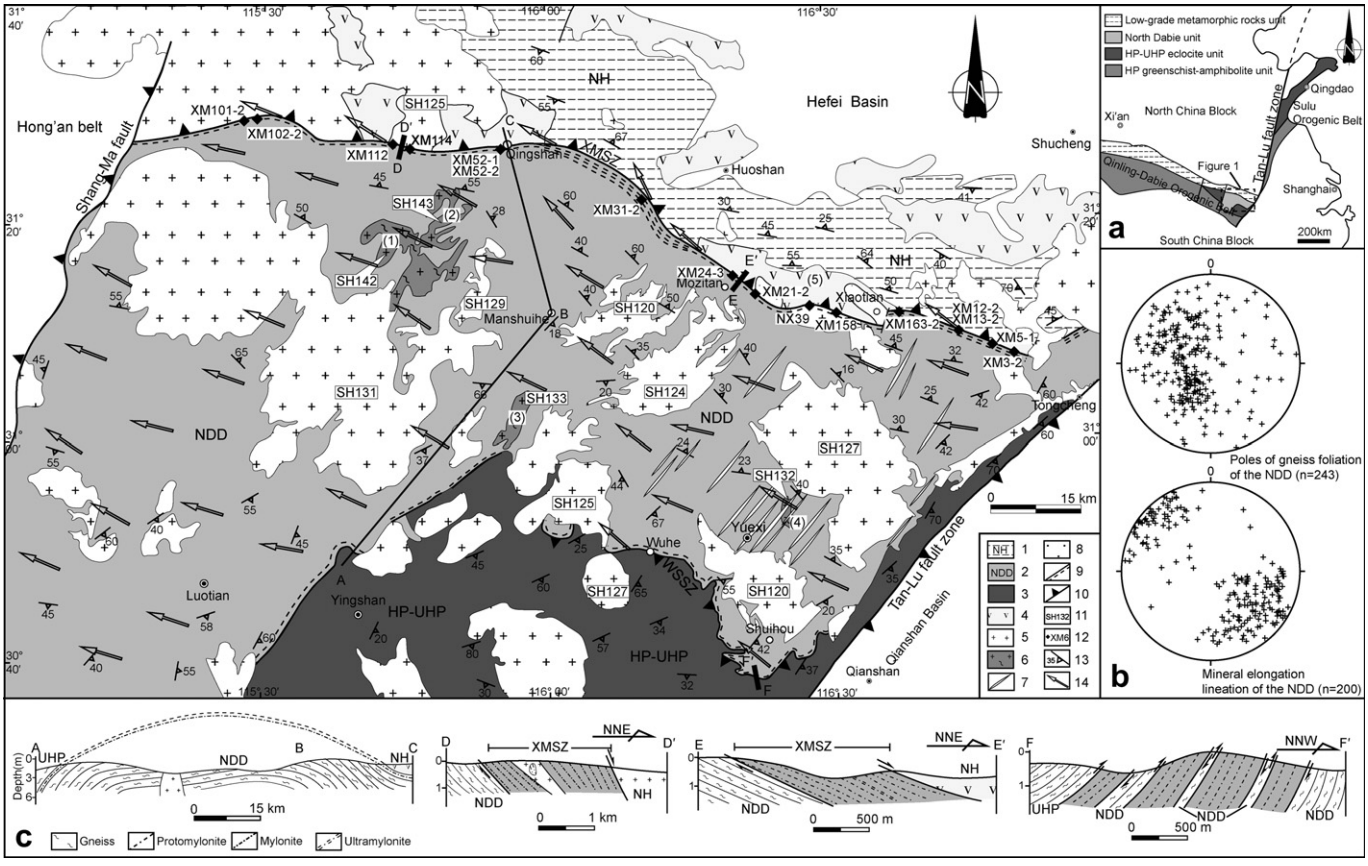

Fig. 1. Structural map of the North Dabie region. Geochronological data for undeformed and deformed intrusions are after Xie et al. (2006), Wang et al. (2007), Xu et al. (2007), and Zhao et al. (2005, 2007). 1: the North Huaiyang unit (NH); 2: the North Dabie Dome (NDD); 3: the UHP eclogite unit (UHP); 4: Early Cretaceous volcanic rocks; 5: Early Cretaceous intrusion (undeformed); 6: Early Cretaceous intrusion (deformed); 7: Early Cretaceous dike; 8: Lower Cretaceous deposits; 9: Ductile shear zone; 10: Brittle normal fault; 11: Zircon SHRIMP U–Pb age; 12: Sampling localities for dating in this paper; 13: Foliation attitude of metamorphic rocks; 14: Top-to-shear sense from field and microscopic observation. (a) Sketch of the Qinling–Dabie-Sulu orogenic belts; (b) Lower-hemisphere, equal-area stereograms of poles to the gneiss foliation and plunges of mineral elongation lineation of the NDD, (c) Cross-sections showing the North Dabie units, the Xiaotian-Mozitan shear zone, and the Wuhe-Shuihou shear zone. NH: northern Huaiyang unit; NDD: northern Dabie dome; UHP: ultra-high pressure unit. (1) The Yunfengding pluton; (2) the Egongbao pluton; (3) the Shigujian pluton; (4) the Shuntan pluton; (5) the Xiaotian Basin.

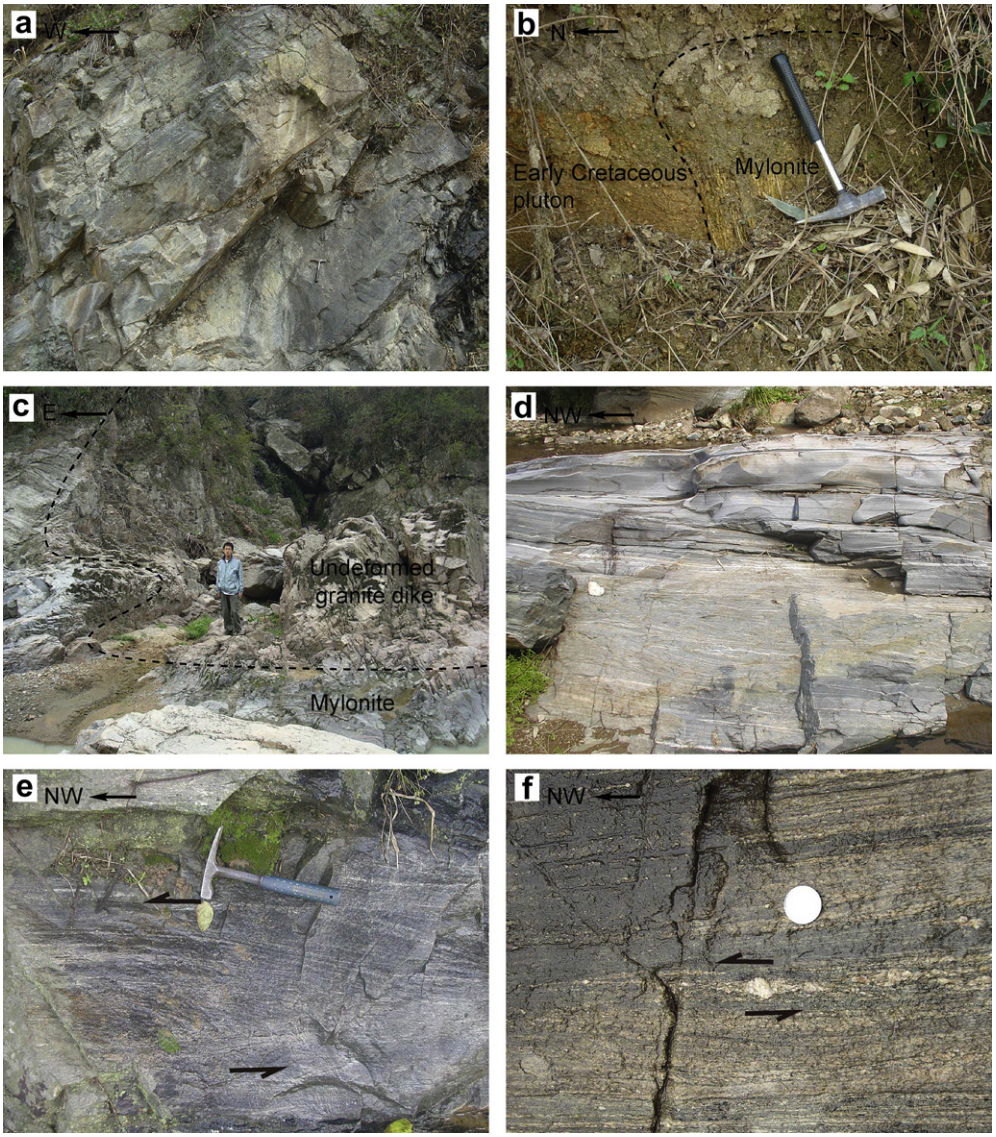

Fig. 2. Field photos from the Xiaotian-Mozitan shear zone. a: Brittle normal faults cut cross the ductile shear zone at a small angle with mylonite foliation; b: Mylonite xenolith in an Early Cretaceous pluton; c: Undeformed granite dike in the ductile shear zone; d: A NW-striking ductile shear belt shown as a mylonite belt; e: S-C fabrics indicating top-to-NW shear sense in the shear zone; f: σ-type feldspar porphyroclast indicating top-to-NW shear sense in the shear zone.

brittle WNW-dipping normal faults. It is a common practice (e.g. Zhai et al., 1995; Suo et al., 2001; Ma et al., 2004; Zhao et al., 2005, 2007; Xu et al., 2007; Wang et al., 2007; Liu et al., 2005a,b; Wu et al., 2007) to divide the DOB, from north to south, into the North Huaiyang unit (NH), the NDD, the ultra-high pressure (UHP) metamorphic unit with coesite-bearing eclogites, the high pressure (HP) metamorphic unit with quartz-bearing eclogites, and the high pressure greenschist-amphibolite facies (HA) metamorphic unit (Fig. 1). Each of these units is briefly described below.

The NH unit east of the Shang-Ma fault zone and north of the XMSZ consists of low-grade metasediments of the Foziling Group and some high-grade orthogneisses with protolith ages of 700–800 Ma (Chen et al., 2003) of the Luzhenguan Group. It is the only unit in the DOB that contains Early Cretaceous volcanic rocks. Zhou et al. (2001) regarded it as an accretionary wedge piece scraped off from the subducted SCB. The Xiaotian Basin, filled with Early Cretaceous terrestrial volcanic and volcanoclastic rocks (Fig. 1), is along the north side of the XMSZ. This basin is bounded by WNW-striking, NNE-dipping normal faults which crosscut the XMSZ (Fig. 1).

The NDD can be divided into two secondary domes: the Luotian dome in the west and the Yuexi dome in the east (Fig. 1). The interior of the NDD is mainly composed of migmatites, high-grade tonalite-trondhjemite-granodiorite (TTG) gneisses and Early Cretaceous granite plutons. Some granulites have been identified in the central and northern part of the Luotian dome (Chen et al., 1998), and are considered to represent lower crustal rocks inside the NDD. The gneisses with protolith ages of 700–800 Ma (Hacker et al., 1998) experienced high-grade metamorphism during the Middle Triassic collision and a subsequent migmatization in the Early Cretaceous (Ratschbacher et al., 2000).

The UHP and HP units (Okay, 1993) in the central DOB consist of orthogneisses and lens of eclogites, jadeite quartzite, marble and garnet pyroxenite. A top-to-NW shear sense in the UHP-HP units is considered to be related to the Late Triassic to Early Jurassic exhumation of the units during collision (Hacker et al., 2000; Faure et al., 2003; Lin et al., 2005). The protolith of these two units yields ages of 700–800 Ma (e.g. Hacker et al., 1998) and thus the two units are interpreted to be derived from the SCB crust. Many geochronological and geochemical data show that they experienced

subduction and peak metamorphism in the Middle Triassic (ca. 235 Ma) followed by exhumation from Late Triassic to Early Jurassic (e.g. Ames et al., 1996; Rowley et al., 1997; Hacker et al., 2000; Li et al., 2000, 2005; Ayers et al., 2002).

The HA unit in southern DOB is separated from the HP unit by the Taihu-Mamiao fault to the north and from the Yangtze foreland fold and thrust belt by the Xiangfan-Guangji fault to the south. The unit is composed of metasediments and orthogneiss metamorphosed to HP greenschist–amphibolite facies during collision (Jiang et al., 2003b). Structures in this unit show a top-to-NW sense of shear, similar to those in the HP-UHP units (Hacker et al., 2000; Lin et al., 2005). Hornblende and muscovite ^{40}Ar–^{39}Ar ages of 228–190 Ma from the unit indicate that it also underwent the collision-related deformation (Hacker and Wang, 1995; Jiang et al., 2003b).

3. Structural analysis and existing geochronological constraints

3.1. Structural features of the XMSZ

The XMSZ extends some 200 km between the Shang-Ma fault and the Tan-Lu fault (Fig. 1) and may extend much further west. It strikes WNW to the east of Mozitan and west of Qingshan, and NW to NNW between Mozitan and Qingshan. Ductile fabrics are pervasive in the XMSZ. Along the northern margin of the XMSZ, later brittle normal faults cut parallel to or at small angles across the mylonite foliation (Fig. 2a). Early Cretaceous volcanic rocks are all limited to basins like the Xiaotian Basin north of the brittle normal faults, indicating that normal faulting controlled the development of these basins. The northern boundary of the XMSZ is partly covered by the Early Cretaceous volcanic rocks in some locations where the exposed width of the zone is narrower (Fig. 1).

Along the ductile XMSZ expose 1 to 2 km wide of protomylonites, mylonites, and locally ultramylonites. The XMSZ gradually transitions into the NDD orthogneiss southwards but is in sharp contact with the NH unit or the undeformed volcanic rocks in the north by brittle normal faults. This indicates that the ductile shear zone overprints the NDD orthogneiss and is overprinted by normal faults. Mylonite xenoliths can also be identified in the undeformed volcanic rocks and in plutons along the XMSZ (Fig. 2b). Some undeformed granite dikes also intruded the ductile shear zone (Fig. 2c).

Mylonitic foliation of the XMSZ dominantly dips at 30–40° to NE or ENE except for the NW- to NNW-striking middle segment where it dips at 30–40° to ENE. Based on the variation in plunge of the stretching lineations, we divide the XMSZ into three segments: the western segment (west of Qingshan), the middle segment (between Qingshan and Mozitan), and the eastern segment (east of Mozitan). In the western segment, the lineation plunges 40–60° NW. In the middle segment, the plunge becomes shallower progressively eastwards until in the eastern segment the lineation is horizontal or sub-horizontal. Outcrop scale kinematic indicators in the XMSZ, such as S-C fabrics (Fig. 2e), σ-type feldspar porphyroclasts (Fig. 2f) and shear bands all show a top-to-NW shear sense.

Observations on oriented thin-sections show that porphyroclasts in the mylonites are dominated by feldspar, hornblende and biotite (Table 1) while the matrix is made of recrystallized quartz, feldspar, biotite, and minor calcite or epidote. Feldspar in mylonites shows widespread dynamic recrystallization by both bulging (BLG) and subgrain rotation (SGR) mechanisms (Fig. 3a and b). In some thin-sections, only BLG recrystallization is observed and the feldspar porphyroclasts display core-mantle structures. Quartz in the

Table 1
Descriptions of the dated mylonite samples from the Xiaotian-Mozitan shear zone and the Wuhe-Shuihou shear zone.

Sample #	Locality	Rock type	Assemblage	Feldspar recrystallization	Quartz recrystallization	Estimated T (°C)
XM3-2	31°07′16.5″N 116°49′19.3″E	Mylonite	P(40%): Feld + Bt M(60%): Qtz + Feld + Bt	BLG	GBM	600±
XM5-1	31°07′20.5″N 116°49′2.2″E	Mylonite	P(45%): Feld + Bt M(55%): Qtz + Feld + Bt	BLG	GBM	600±
XM12-2	31°08′22.8″N 116°45′47.6″E	Mylonite	P(30%): Feld + Hb M(70%): Qtz + Feld + Bt + Cal	BLG + SGR	GBM	650±
XM13-2	31°08′12.7″N 116°45′32.5″E	Protomylonite	P(55%): Feld + Hb M(45%): Qtz + Feld + Bt + Ep	BLG + SGR	GBM	650±
XM21-2	31°13′29.9″N 116°22′17.2″E	Mylonite	P(40%): Feld + Hb M(60%): Qtz + Feld + Bt	BLG + SGR	GBM	650±
XM24-3	31°15′18.3″N 116°19′50.9″E	Protomylonite	P(55%): Feld + Hb + Bt M(45%): Qtz + Feld + Bt	BLG + SGR	GBM	650±
XM31-2	31°21′1.2″N 116°10′18.3″E	Protomylonite	P(60%): Feld + Hb + Bt M(40%): Qtz + Feld + Bt	BLG	GBM	600±
XM52-1	31°25′15.1″N 115°55′41.0″E	Protomylonite	P(60%): Feld + Hb + Bt M(40%): Qtz + Feld + Bt	BLG + SGR	GBM	650±
XM52-2	31°25′15.1″N 115°55′41.0″E	Protomylonite	P(65%): Feld + Hb + Bt M(35%): Qtz + Feld + Bt	BLG + SGR	GBM	650±
XM101-2	31°29′11.7″N 115°29′11.7″E	Protomylonite	P(55%): Feld + Bt M(45%): Qtz + Feld + Bt	BLG	GBM	600±
XM102-2	31°26′50.3″N 115°28′45.4″E	Mylonite	P(45%): Feld + Bt M(55%): Qtz + Feld + Bt	BLG	GBM	600±
W2-1	30°41′49.9″N 116°23′33.5″E	Protomylonite	P(70%): Feld + Hb + Bt M(30%): Qtz + Feld + Bt	BLG + SGR	GBM	650±
W5-1	30°42′20.3″N 116°23′08.0″E	Protomylonite	P(65%): Feld + Bt M(35%): Qtz + Feld + Bt	BLG	GBM	600±
W9	30°43′27.9″N 116°19′54.0″E	Mylonite	P(45%): Feld + Hb M(55%): Qtz + Feld + Bt	BLG + SGR	GBM	650±
W13	30°43′13.6″N 116°20′19.6″E	Mylonite	P(40%): Feld + Hb + Bt M(60%): Qtz + Feld + Bt	BLG + SGR	GBM	650±

P, porphyroclasts; M, matrix; Qtz, quartz; Feld, feldspar; Ms, muscovite; Bt, biotite; Cal, calcite; Ep, epidote; BLG, bulging recrystallization; SR, subgrain rotation recrystallization; GBM, grain boundary migration recrystallization.

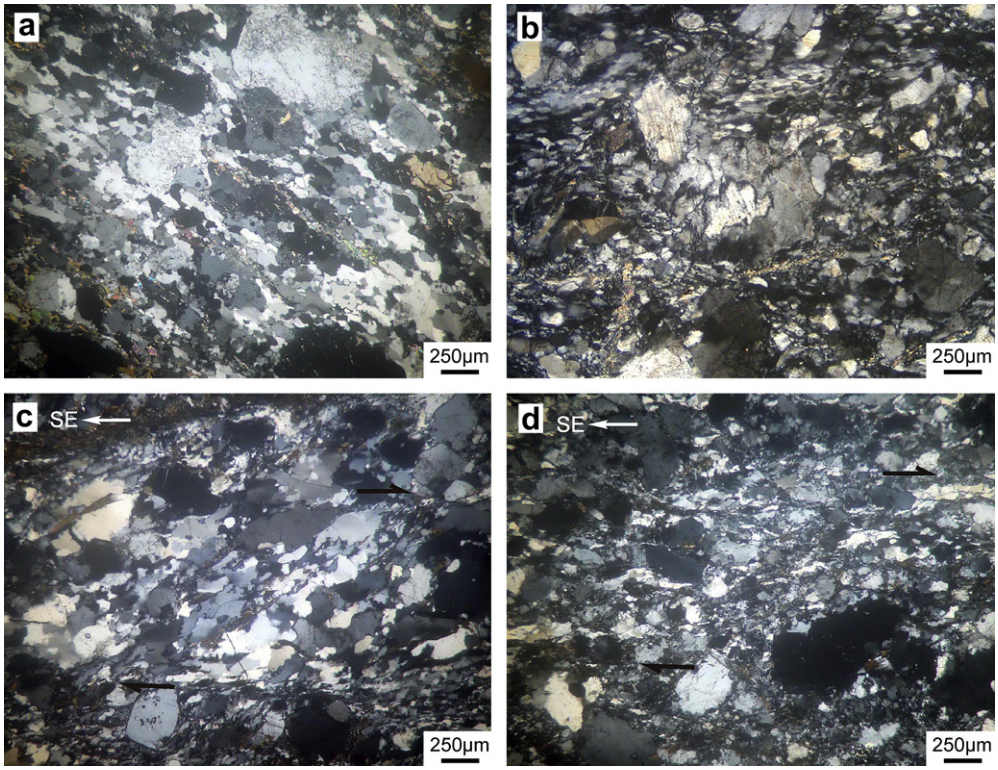

Fig. 3. Photomicrographs of dated mylonite samples from the Xiaotian-Mozitan shear zone. All thin-sections are cut parallel with XZ plane. Field of view = 3 mm. Crossed polarizers. Sample localities are shown in Fig. 1. a: XM21-1 mylonite, coexistence of feldspar BLG and SGR recrystallization; b: XM5-1 mylonite, feldspar mainly by SGR recrystallization; c: XM31-2 protomylonite, S-C fabrics formed by SGR recrystallizated feldspar grains, indicating top-to-NW sense of shear; d: XM24-3 protomylonite, S-C fabrics shown by GBM recrystallizated quartz and SGR recrystallizated feldspar grains, indicating top-to-NW sense.

mylonite is widely recrystallized by the grain boundary migration (GBM) mechanism (Fig. 3c), indicating a regime 3 dislocation creep (Hirth and Tullis, 1992). Two generations of biotite grains are commonly observed. The newly-formed, finer-grained biotite grains in the matrix have a short axis of ca. 10 μm and the porphyroclastic biotite grains have a short axis >150 μm. Microstructures such as S-C fabrics (Fig. 3c and d) and obliquely arranged minerals in oriented thin-sections also indicate a top-to-NW or NWW shear sense.

To further confirm the shear sense of the XMSZ, we analyzed the quartz c-axis fabric on sixteen oriented mylonite samples. c-axis orientations were measured using a U-stage and results are plotted using StereoNett 2.46. As shown in Fig. 4, half of quartz c-axis patterns of the XMSZ show a mixture of monoclinic symmetry and orthorhombic symmetry and dominated by monoclinic symmetry. The c-axis patterns all show an asymmetry with respect to the minimum axis of the finite strain ellipsoid, suggesting a top-to-NW or WNW shear sense, consistent with field and microscopic observations.

3.2. Interior of the NDD

Rock types inside the NDD include migmatite, migmatitic gneiss (Fig. 5a) and locally granulite. Previous work demonstrates that they have also experienced collision-related metamorphism during 218–209 Ma (Liu et al., 2007). Relics of UHP eclogites that have experienced conditions of $T \geq 750$–800 °C and $P \sim 3.5$ GPa have been reported locally (Xu et al., 2003; Malaspina et al., 2006; Lin et al., 2007) but most of such rocks have been eroded from the top of the dome.

Previous work has documented that structures inside the NDD have a top-to-NW or WNW shear sense (Hacker et al., 2000; Faure et al., 2003; Lin et al., 2007). Our more detailed field investigation also shows that the stretching lineations in the NDD plunge WNW or ESE (Fig. 1b), and shear sense indicators such as σ-type feldspar porphyroclasts, S-C fabrics, shear folds (Fig. 5b) and rotated mafic blocks (Fig. 5c) inside the NDD all indicate a top-to-NW or WNW shear sense (Fig. 1). Gneissic foliation in the northern part of the dome, such as along the transverse north of Manshuihe in Fig. 1, dips north or northeast whereas in the southern part the foliation dips south or southeast, exhibiting an antiformal shape as a whole. The foliation near the Tan-Lu fault zone strikes NE and dips SE. Stretching lineation plunge decreases from the middle part of the dome to the northern margin. The lineation plunges ESE around the WSSZ. Foliation in the middle part of the dome shows variable strikes and dip angles while the lineation consistently plunges WNW or ESE. This geometry suggests that the high-grade rocks in the NDD were all affected by the ductile deformation with a top-to-NW or WNW sense of shear. The gneisses inside the NDD have many isoclinal, intrafolial folds with their axial planes parallel to the gneiss foliation in the outcrop (Fig. 5b).

Large Early Cretaceous granite plutons occur in the NDD (Fig. 1). The plutons of the earlier stage (older than 132 Ma and with an available oldest zircon age of 143 Ma) are adakitic granite whereas those of the later stage (younger than 129 Ma) are non-adakitic (e.g. Wang et al., 2007; Xu et al., 2007; Huang et al., 2008). It has been proposed that the NDD had a thicker >50 km crust before 132 Ma and normal <35 km crust after 129 Ma (Wang et al., 2007; Xu et al., 2007; Huang et al., 2008). Our field investigation shows that the smaller earlier stage plutons (Fig. 1), such as the Yunfengding, Egongbao, Shigujian and Shuntan, were deformed with a penetrative foliation (Fig. 5d) whereas those larger later stage plutons are undeformed. The Yunfengding monzogranite yielding an oldest

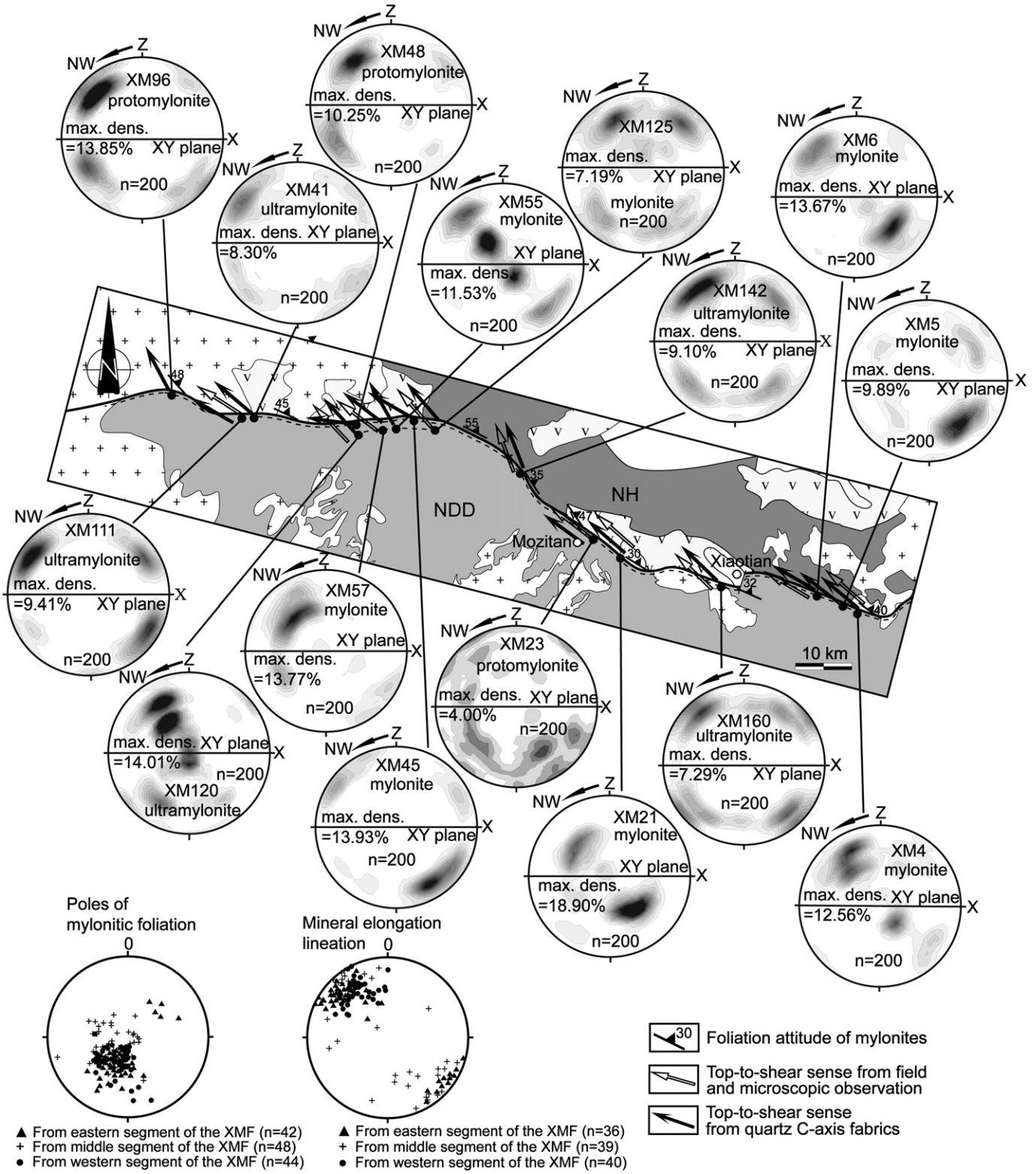

Fig. 4. Quartz c-axis stereograms of dynamically recrystallized quartz in mylonites from the Xiaotian-Mozitan shear zone. Contours are 1, 2, up to 19% per 1% area. Lower-hemisphere, equal-area projection. The thin-sections are parallel with XZ plane. X, Y, Z are principle axes of finite strain. *n*: measured grain numbers.

zircon age of 143 Ma is clearly deformed with a well-developed foliation dominantly dipping at 30–40°SE and a lineation defined by elongated feldspars plunging about 20°ESE. Kinematic indicators in the pluton such as σ-type feldspar porphyroclasts show a top-to-WNW shear sense. Similar structures are also present in the Egongbao pluton with a zircon age of 142 Ma (Wang et al., 2007). The Shigujian and Shuntan plutons with zircon ages of 133 Ma and 132 Ma (Xu et al., 2007) respectively, exhibit even stronger deformation than the Yunfengding and Egongbao plutons. Foliation in the Shigujian and Shuntan plutons dominantly dips at

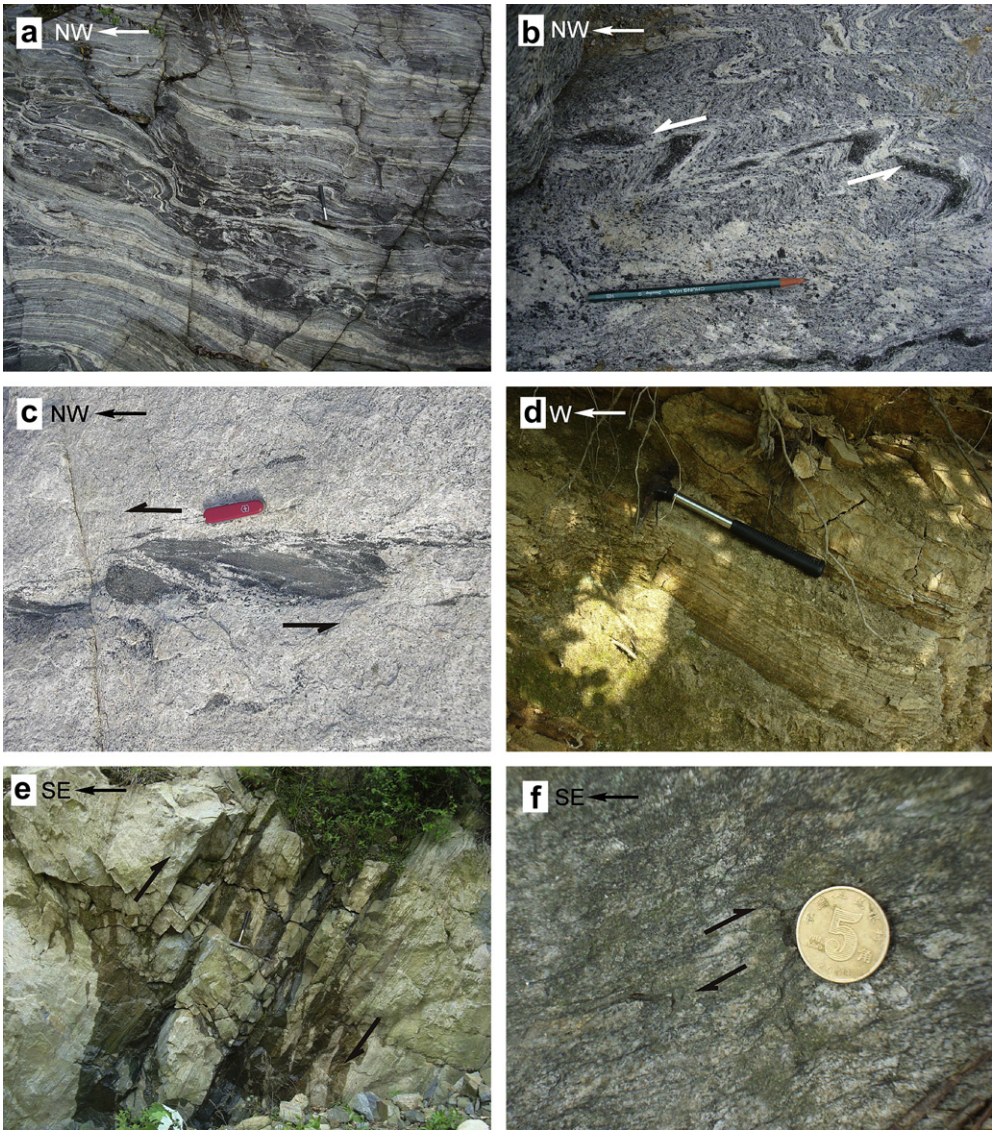

Fig. 5. Field photos from the North Dabie dome and the Wuhe-Shuihou shear zone. a: The migmatitic gneisses in Manshuihe of the North Dabie dome; b: Tight to isoclinal fold near Sipohe of the North Dabie dome, indicating top-to-NW sense of shear; c: Deformed mafic block in the migmatitic gneisses of the North Dabie dome, indicating top-to-NW sense of shear; d: Monzogranite in Yunfengding pluton with well-developed foliation; e: Ductile shear zone of about 5 m wide in the Wuhe-Shuihou shear zone, overprinting on gneisses of the North Dabie dome; f: σ-type feldspar porphyroclast in the Wuhe-Shuihou shear zone, indicating top-to-NW shear sense.

40–50°NE and the lineation plunges 10–20°NW. Kinematic indicators in the two plutons also show a top-to-NW shear sense. The foliation of these deformed plutons can be traced to their country gneisses. All of the deformed plutons show fabrics and shear senses similar to their country gneisses, indicating that both were deformed in the same tectonic event.

Metamorphosed rocks and deformed intrusions inside the NDD have been well dated by the $^{40}Ar-^{39}Ar$ and zircon U–Pb methods (Eide et al., 1994; Hacker and Wang, 1995; Ratschbacher et al., 2000; Wang et al., 2007; Wu et al., 2007; Xu et al., 2007). Available $^{40}Ar-^{39}Ar$ ages of hornblende, muscovite and biotite and zircon margin U–Pb ages range from 143 Ma to 110 Ma, suggesting that ductile, top-to-NW or WNW sense shearing inside the NDD took place in the Early Cretaceous. Wu et al. (2007) obtained a 137 Ma U–Pb SHRIMP age of metamorphosed zircon from the migmatitic gneiss inside the NDD, also suggesting that migmatization and associated deformation inside the NDD took place in the earliest Early Cretaceous time.

3.3. Structural features of the WSSZ

The WSSZ is overlain by the UHP slab to the south (Wang et al., 1995; Zhai et al., 1995; Ratschbacher et al., 2000; Jiang et al., 2003a; Lin et al., 2007) and its protolith are gneisses of the NDD. The west part of this zone (west of Wuhe) is poorly exposed. Our work was focused on the well-exposed east part near Shuihou. There the WSSZ occurs as several ductile shear zones, each of which ranges from tens to several hundred meters in width. The shear zones are composed of protomylonites, mylonites and locally ultramylonites, which overprint the NDD gneisses (Fig. 5e). The mylonitic foliation of the shear zones has variable strikes but dominantly dips SE at 40–50° (Fig. 6). Stretching lineations in the mylonites dominantly plunge SE at around 45°. S-C structures and σ-type feldspar porphyroclasts (Fig. 5f) in the shear zones indicate a top-to-NW or WNW shear sense, which is consistent with the previous studies (e.g. Hacker et al., 1995, 2000; Faure et al., 1999; Ratschbacher et al., 2000; Jiang et al., 2003a). Ratschbacher et al. (2000) obtained

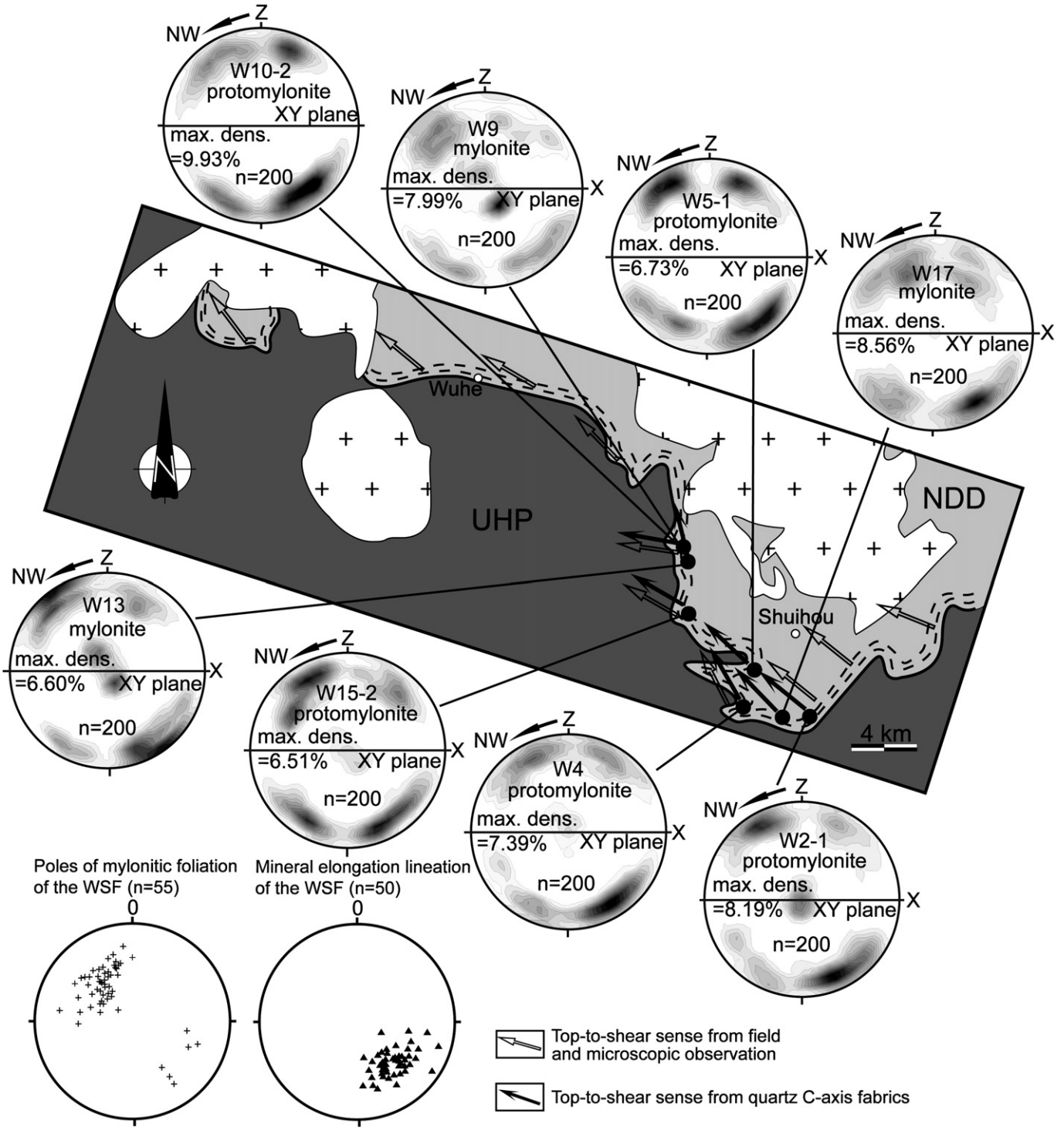

Fig. 6. Quartz c-axis stereograms of dynamically recrystallized quartz in mylonites from the Wuhe-Shuihou shear zone. Contours are 1, 2, up to 10% per 1% area. Lower-hemisphere, equal-area projection. The thin-sections are parallel with XZ plane. X, Y, Z are principle axes of finite strain. *n*: measured grain numbers.

a biotite ^{40}Ar—^{39}Ar age of 126 Ma and a muscovite ^{40}Ar—^{39}Ar age of 130 Ma along the WSSZ and interpreted them as representing the cooling ages of the WSSZ.

Observations on oriented thin-sections show that porphyroclasts in mylonites of the WSSZ, like those from the XMSZ, are also dominated by feldspars, hornblendes, and biotites. Matrices of the mylonites are fine-grained, recrystallized quartz, feldspar, biotite, and epidote. Recrystallization mechanisms of feldspar are BLG and SGR while quartz only shows GBM recrystallization. S-C fabrics (Fig. 3c and d) and σ-type feldspar porphyroclasts in oriented thin-sections also indicate a top-to-NW or WNW shear sense.

We analyzed quartz c-axis fabrics on eight oriented mylonite samples from the WSSZ. As shown in Fig. 6, all the c-axis patterns exhibit mixture of monoclinic symmetry and orthorhombic symmetry and dominated by monoclinic symmetry. The c-axis patterns, with respect to the minimum axis of the finite strain

ellipsoid, also indicate a top-to-NW shear sense which is consistent with our field and microscopic observations.

3.4. Deformation temperatures

Syn-kinematic mineral assemblages and mineral deformation characteristics in mylonites can be used to estimate the deformation temperature. In naturally deformed rocks, quartz recrystallizes by the GBM recrystallization at 500 °C and above (Stipp et al., 2002). Recrystallization of feldspar starts at 500 °C, BLG at 500–650 °C, and BLG transitional with SGR at 650–700 °C, solely SGR at 700–800 °C, SGR transitional with GBM at 800–850 °C, and solely GBM at 850 °C and above (Tullis and Yund, 1991; Pryer, 1993; Altenberger, 2000). Quartz in mylonites from both the XMSZ and the WSSZ is dominated by GBM recrystallization, while feldspar mostly shows coexistence of BLG and SGR recrystallization and some exhibit dominant BLG recrystallization (Table 1). All this suggests that the deformation temperatures were about 600–650 °C.

4. Geochronology of the XMSZ

4.1. ^{40}Ar–^{39}Ar dating for the XMSZ

Seven biotite and seven hornblende samples from mylonites of the XMSZ were separated by means of the standard separation techniques for ^{40}Ar–^{39}Ar dating. On the basis of microscopic observation, size fractions of >105 μm were used to obtain porphyroclastic biotite and hornblende. The biotite and hornblende in the matrix mostly are a few micrometers wide. They have quite low closure temperatures (Dodson, 1973; Reddy and Potts, 1999) and are thus not suitable for dating.

The mineral separates were irradiated in the H8 position of the Swimming Pool Reactor at the Institute of Atomic Energy, Chinese Academy of Sciences, Beijing. The monitor used in this study is the Fangshan standard biotite (ZBH-25) with an age of 132.7 ± 1.2 Ma and potassium content of 7.6%. ^{40}Ar–^{39}Ar analyses of the samples were conducted with an MM-1200B Mass Spectrometer at the Ar–Ar Laboratory, Institute of Geology, Chinese Academy of Geological Sciences, Beijing. Measured isotopic ratios were corrected for mass discrimination, atmospheric Ar component, blanks, and irradiation induced mass interference. The correction factors of interfering isotopes produced during irradiation were determined by the analysis of irradiated K_2SO_4 and CaF_4 pure salts and their values are: $(^{36}Ar/^{37}Ar)_{Ca} = 0.000240$; $(^{40}Ar/^{39}Ar)_k = 0.004782$; $(^{39}Ar/^{37}Ar)_{Ca} = 0.000806$. The blanks of the $m/e = 40$, $m/e = 39$, $m/e = 37$, $m/e = 36$ are less than 6×10^{-15} mol, 4×10^{-16} mol, 8×10^{-17} mol and 2×10^{-17} mol respectively. The ^{40}Ar–^{39}Ar analytical data are listed in Table 2, and their age spectra, total gas ages (TGA), plateau ages (t_p) and inverse isochron date were defined and calculated using the program ISOPLOTS3.14 (Ludwig, 2004). All errors are quoted at the 1σ level.

As shown in Fig. 7, all samples except biotite XM3-2 yield a plateau age. The cumulative $\%^{39}Ar$ released of flat plateaus of biotite XM3-2 is less than 60% of the total $\%^{39}Ar$ released (Ludwig, 2004). A weighted mean age (t_w) of the biotite for higher temperature steps is 136.5 ± 1.3 Ma. The six biotite samples with plateau ages give plateau ages (t_p) ranging from 120.7 ± 0.7 Ma to 130.7 ± 1.0 Ma. The seven hornblende samples yield plateau ages ranging from 127.0 ± 0.8 Ma to 141.9 ± 1.2 Ma. For each sample, its total gas age (TGA), t_p and inverse isochron age (t_i) are consistent within errors except for hornblende samples of XM12-2, XM21-2, XM24-3 and XM52-2 with t_p slightly older than t_i. Initial $^{40}Ar/^{36}Ar$ values (Table 2) of all samples are close to the atmospheric ratio of 295.5 whereas their MSWD range from 5.8 to 0.5. Therefore, the obtained plateau ages are considered to be reliable.

4.2. Dating of undeformed granite dikes in the XMSZ

To further constrain the age of deformation of the XMSZ, four granite dikes samples were collected for U–Pb zircon LA-ICPMS dating. These dikes are undeformed and cut across the XMSZ (Fig. 2c). Therefore, they postdate the ductile deformation of the XMSZ.

Cathodoluminescence (CL) images (Fig. 8) of zircon grains separated from the granite dike were acquired using a Quanta 400FEG environmental scanning electron microscope (ESEM) equipped with an Oxford energy dispersive spectroscopy (EDS) system and a Gatan CL3+ CL detector at the Department of Geology, Northwest University, China. Most of the images show igneous, oscillatory growth zoning which is consistent with their high Th/U ratios, suggesting a magmatic origin. Laser ablation ICPMS (LA-ICPMS) U–Pb analyses of 67 zircon grains from the 4 dike samples (Table 3) were conducted on an Elan 6100 DRC ICPMS equipped with 193 nm laser also at the Department of Geology, Northwest University in Xi'an, China. Zircon 91500 was used as a standard and the standard silicate glass NIST was used to optimize the machine. The analytical technique is described in detail by Wu et al. (2005). Errors on individual analyses by LA-ICPMS are quoted at the 1σ level.

Analyses of the zircon samples NX39 and XM158 from the eastern segment of the XMSZ yield $^{206}Pb/^{238}U$ weighted mean ages of 120.9 ± 1.1 Ma and 120.0 ± 1.0 Ma respectively (MSWD = 0.4, Fig. 8). Analyses of the zircon samples XM112 and XM114 from the western segment of the XMSZ give $^{206}Pb/^{238}U$ weighted mean ages of 129.3 ± 1.1 Ma, 129.9 ± 1.3 Ma and MSWD = 0.7, 0.5, respectively, (Fig. 8). These ages are interpreted as the intrusion ages of the four granite dikes in the XMSZ. The results indicate that the ductile shearing ended before 130 Ma in the western segment of the XMSZ and before 121 Ma in its eastern segment.

5. Discussion

5.1. Formation time of the XMSZ

To understand the implications of the obtained ^{40}Ar–^{39}Ar ages, the relationship between deformation and closure temperatures of dated minerals must be considered. If a deformation event occurs at a temperature higher than the closure temperature of a dated mineral, the obtained age represents a cooling age (Dodson, 1973). In this work, the deformation temperatures of the dated mylonites are between 600 and 650 °C (Table 1), higher than the closure temperatures of hornblende (500 ± 50 °C, Harrison, 1981) and biotite (300 ± 50 °C, Hacker and Wang, 1995). Argon system in these minerals would have been totally reset. We therefore interpret the obtained ages of porphyroclastic biotite and hornblende as representing the cooling ages following the deformation event.

Since hornblende has a higher closure temperature for Ar system than biotite, hornblende ages are therefore closer to the real deformation age. Our ^{40}Ar–^{39}Ar dating results also show that the obtained hornblende plateau ages (127 Ma–142 Ma) are older than the biotite plateau ages (121 Ma–131 Ma) from the same samples (Table 2, Fig. 7). The oldest cooling age obtained is a plateau age of 141.9 ± 1.2 Ma (the earliest Early Cretaceous) for the hornblende sample XM31-2. Based on this, we believe that the ductile shearing along the XMSZ probably took place in the earliest Early Cretaceous, prior to 142 Ma. The shearing terminated before 130 Ma in the western segment and before 121 Ma in the eastern segment of

Table 2
Detailed $^{40}Ar-^{39}Ar$ analytical results.

T(°C)	$(^{40}Ar/^{39}Ar)_m$	$(^{36}Ar/^{39}Ar)_m$	$(^{37}Ar/^{39}Ar)_m$	$(^{38}Ar/^{39}Ar)_m$	$^{40}Ar^*/^{39}Ar$	^{39}Ar/%	Age ± 1σ/Ma
XM3-2 biotite, $W = 0.050$ g, $J = 0.011481$, TGA = 118.6 ± 4.5 Ma, $t_w = 136.5 \pm 1.3$ Ma (9–12 steps, 48.6% released ^{39}Ar), $t_i = 136.2 \pm 2.8$ Ma, initial $^{40}Ar/^{36}Ar = 292.5 \pm 8.1$, MSWD = 1.6							
500	202.48	0.6829	9.1888	0.1428	1.35	5.08	28.0 ± 10
600	132.97	0.4492	0.7922	0.0960	0.28	1.24	5.7 ± 4.7
700	104.01	0.3477	0.4880	0.0774	1.29	4.40	26.0 ± 15
800	33.406	0.0914	0.4768	0.0296	6.42	2.13	128.2 ± 8.2
900	18.618	0.0406	0.1034	0.0188	6.61	10.2	132.0 ± 3.9
1000	18.529	0.0390	0.2342	0.0173	7.03	4.81	140.0 ± 5.4
1100	31.435	0.0875	0.2221	0.0300	5.58	14.5	112.1 ± 5.8
1200	37.376	0.1069	0.9056	0.0327	5.85	9.05	117.2 ± 5.6
1250	20.975	0.0484	0.2141	0.0210	6.68	9.89	133.2 ± 3.3
1300	11.448	0.0157	0.2426	0.0152	6.82	15.2	136.0 ± 2.0
1350	9.3026	0.0081	0.3708	0.0141	6.94	16.3	138.3 ± 1.8
1400	8.8827	0.0074	1.5549	0.0146	6.81	7.16	135.9 ± 2.3
XM5-1-1 biotite, $W = 0.045$ g, $J = 0.005047$, TGA = 126.1 ± 1.6 Ma, $t_P = 129.8 \pm 0.6$ Ma (7–11 steps, 86.9% released ^{39}Ar), $t_i = 129.9 \pm 1.5$ Ma, initial $^{40}Ar/^{36}Ar = 296 \pm 39$, MSWD = 0.9							
500	17.110	0.0316	0.1185	0.0837	7.76	0.47	69.3 ± 5.5
600	18.906	0.0399	0.0840	0.0696	7.10	0.42	63.5 ± 5.4
700	20.834	0.0584	0.2341	0.1349	3.58	0.23	32.0 ± 19
800	18.805	0.0590	0.1615	0.0922	1.38	0.77	13.0 ± 12
900	18.872	0.0358	0.0407	0.0267	8.30	2.62	74.0 ± 1.4
1000	16.754	0.0095	0.0099	0.0159	13.9	8.62	122.7 ± 1.8
1070	17.375	0.0088	0.0058	0.0144	14.8	10.53	129.7 ± 1.5
1140	15.716	0.0026	0.0065	0.0144	14.9	9.1	131.1 ± 1.6
1200	16.076	0.0043	0.0082	0.0154	14.8	10.99	129.9 ± 1.7
1300	15.252	0.0016	0.0060	0.0069	14.8	46.88	129.8 ± 1.3
1400	15.142	0.0016	0.0046	0.0145	14.7	9.37	128.8 ± 1.4
XM5-1-2 biotite, $W = 0.052$ g, $J = 0.011846$, TGA = 123.8 ± 1.8 Ma, $t_P = 129.2 \pm 1.0$ Ma (4–13 steps, 95.8% released ^{39}Ar), $t_i = 129.3 \pm 3.0$ Ma, initial $^{40}Ar/^{36}Ar = 297 \pm 13$, MSWD = 1.5							
500	113.36	0.3502	1.2716	0.0889	9.97	0.92	201 ± 30
600	79.638	0.2672	0.2371	0.0651	0.69	2.61	14.6 ± 8.9
700	35.326	0.1031	0.9155	0.0349	4.94	0.71	102.5 ± 8.8
800	14.656	0.0279	0.0887	0.0180	6.41	9.52	132.1 ± 2.3
900	12.460	0.0215	0.1223	0.0168	6.12	5.89	126.2 ± 2.6
1000	8.7489	0.0083	0.0528	0.0143	6.30	7.43	129.9 ± 1.9
1100	9.7795	0.0119	0.0639	0.0151	6.26	15.3	129.0 ± 2.1
1150	9.6551	0.0110	0.1595	0.0151	6.42	4.43	132.2 ± 2.9
1200	8.6187	0.0079	0.0836	0.0141	6.30	7.24	129.8 ± 1.8
1250	7.7261	0.0050	0.0521	0.0140	6.25	13.31	128.8 ± 1.5
1300	7.6243	0.0048	0.0460	0.0132	6.21	16.5	128.1 ± 1.4
1350	8.3950	0.0074	0.0821	0.0141	6.21	11.3	128.0 ± 1.4
1400	8.9805	0.0086	0.2909	0.0144	6.46	4.82	133.0 ± 2.4
XM12-2 hornblende, $W = 0.261$ g, $J = 0.011832$, TGA = 143.8 ± 3.3 Ma, $t_P = 133.1 \pm 0.9$ Ma (5–12 steps, 88.7% released ^{39}Ar), $t_i = 127.4 \pm 0.9$ Ma, initial $^{40}Ar/^{36}Ar = 290.3 \pm 4.2$, MSWD = 0.9							
500	37.766	0.0869	12.754	0.0658	13.1	5.13	260.5 ± 6.1
600	99.310	0.3094	23.601	0.1133	9.72	2.83	196.0 ± 30
700	82.252	0.2674	28.133	0.1123	5.36	1.49	111.0 ± 24
800	33.452	0.0711	4.8963	0.0435	12.9	1.81	255.3 ± 6.3
900	31.572	0.0868	6.8934	0.0424	6.43	0.78	132.3 ± 9.8
1000	20.820	0.0529	7.8696	0.0335	5.77	1.15	119.2 ± 4.0
1080	15.906	0.0335	6.6367	0.0229	6.49	3.54	133.5 ± 3.3
1130	7.9298	0.0061	5.1534	0.0153	6.50	14.0	133.8 ± 1.6
1180	7.9284	0.0060	4.8329	0.0147	6.52	27.2	134.0 ± 1.7
1230	7.9742	0.0061	4.6643	0.0147	6.51	9.16	133.9 ± 1.5
1300	8.1809	0.0067	4.2953	0.0144	6.52	25.2	134.1 ± 2.0
1400	7.8550	0.0059	4.6276	0.0146	6.45	7.81	132.6 ± 1.5
XM13-2 hornblende, $W = 0.293$ g, $J = 0.011832$, TGA = 138.0 ± 2.1Ma, $t_P = 134.1 \pm 0.9$ Ma (6–12 steps, 92.6% released ^{39}Ar), $t_i = 130.9 \pm 5.7$ Ma, initial $^{40}Ar/^{36}Ar = 245 \pm 43$, MSWD = 3.0							
500	58.663	0.1674	18.378	0.0783	10.7	1.78	215.0 ± 15
600	35.708	0.0800	8.3717	0.0457	12.8	1.91	253.4 ± 6.3
700	36.635	0.1130	12.096	0.0550	4.13	0.74	86.0 ± 12
800	27.936	0.0800	7.9562	0.0425	4.88	1.05	101.0 ± 11
900	18.165	0.0310	3.6210	0.0265	9.28	1.96	187.9 ± 4.9
1000	16.674	0.0352	7.1993	0.0305	6.82	1.84	140.1 ± 3.1
1080	8.9937	0.0098	4.7892	0.0168	6.47	7.27	133.1 ± 1.9
1130	7.2372	0.0034	4.5350	0.0148	6.56	16.9	134.8 ± 1.5
1180	6.8547	0.0024	4.3277	0.0145	6.47	34.2	133.0 ± 1.4
1230	7.0592	0.0029	4.4146	0.0147	6.53	11.1	134.3 ± 1.6
1300	7.0264	0.0028	4.4045	0.0146	6.53	20.8	134.3 ± 1.5
1400	9.4264	0.0133	10.327	0.0282	6.28	0.41	129.3 ± 4.3

(*continued on next page*)

Table 2 (*continued*)

T(°C)	$(^{40}Ar/^{39}Ar)_m$	$(^{36}Ar/^{39}Ar)_m$	$(^{37}Ar/^{39}Ar)_m$	$(^{38}Ar/^{39}Ar)_m$	$^{40}Ar^*/^{39}Ar$	^{39}Ar/%	Age ± 1σ/Ma
XM21-2 hornblende, W = 0.297 g, J = 0.011828, TGA = 141.9 ± 2.6Ma, t_P = 136.8 ± 1.1 Ma (9–12 steps, 67.1% released ^{39}Ar), t_i = 123.0 ± 2.2 Ma, initial $^{40}Ar/^{36}Ar$ = 338 ± 160, MSWD = 2.9							
500	46.750	0.1001	9.7969	0.0535	18.0	1.41	348.0 ± 9.3
600	116.851	0.3585	5.8104	0.0895	11.4	0.94	227.0 ± 21
700	55.456	0.1589	5.5651	0.0482	8.94	1.37	181.0 ± 14
800	30.640	0.0818	1.7615	0.0301	6.59	2.74	135.4 ± 4.3
900	24.962	0.0622	0.7461	0.0258	6.62	3.54	136.0 ± 3.9
1000	35.539	0.1022	1.2447	0.0333	5.44	4.38	112.5 ± 4.2
1080	29.819	0.0789	2.8437	0.0308	6.72	5.55	138.0 ± 6.2
1130	10.4574	0.0117	5.0779	0.0221	7.38	13.0	151.0 ± 2.0
1180	7.7583	0.0051	5.4183	0.0214	6.66	28.2	136.8 ± 1.5
1230	7.6580	0.0054	5.3575	0.0217	6.48	19.5	133.2 ± 1.5
1300	9.3783	0.0102	5.7588	0.0224	6.81	10.9	139.7 ± 1.9
1400	8.5643	0.0073	5.6117	0.0224	6.82	8.56	140.0 ± 1.8
XM24-3 biotite, W = 0.049 g, J = 0.011716, TGA = 144.4 ± 3.0 Ma, t_P = 130.7 ± 1.0 Ma (4–12 steps, 84.5% released ^{39}Ar), t_i = 129.2 ± 2.3 Ma, initial $^{40}Ar/^{36}Ar$ = 294 ± 5.3, MSWD = 1.9							
400	13.148	0.0307	49.411	0.2177	7.89	5.16	161.7 ± 5.1
500	21.949	0.0264	7.5238	0.0472	14.8	4.23	291.4 ± 4.0
600	36.100	0.0847	4.2177	0.0454	11.4	6.12	229.2 ± 5.4
700	55.921	0.1682	1.4648	0.0503	6.34	3.65	130.9 ± 9.8
800	52.871	0.1579	0.9512	0.0453	6.27	1.45	129.7 ± 8.5
900	12.136	0.0202	0.0847	0.0176	6.16	21.0	127.5 ± 2.9
950	9.7497	0.0112	0.0857	0.0156	6.43	6.02	132.8 ± 1.9
1000	11.026	0.0163	0.2360	0.0170	6.23	4.05	128.7 ± 2.5
1100	12.285	0.0198	0.2209	0.0438	6.45	6.45	133.2 ± 2.8
1200	9.3765	0.0102	0.1082	0.0154	6.37	11.9	131.6 ± 1.6
1300	9.6700	0.0115	0.0386	0.0154	6.26	26.3	129.3 ± 1.7
1400	10.177	0.0131	0.2508	0.0161	6.33	3.72	130.7 ± 2.1
XM24-3 hornblende, W = 0.285 g, J = 0.011828, TGA = 123.9 ± 1.7 Ma, t_P = 132.0 ± 0.8 Ma (6–12 steps, 93.8% released ^{39}Ar), t_i = 123.9 ± 1.4 Ma, initial $^{40}Ar/^{36}Ar$ = 298.8 ± 3.4, MSWD = 1.5							
500	75.137	0.2317	5.2144	0.0703	7.05	0.76	145.0 ± 19
600	52.088	0.1602	4.2462	0.0489	5.05	0.67	105.0 ± 11
700	26.793	0.0701	1.4713	0.0288	6.20	1.02	127.6 ± 6.2
800	22.982	0.0572	1.1844	0.0256	6.17	1.84	127.1 ± 6.1
900	18.950	0.0389	1.1342	0.0209	7.55	1.89	154.3 ± 4.5
1000	20.835	0.0493	1.8616	0.0230	6.39	2.26	131.5 ± 3.0
1080	21.370	0.0518	3.1868	0.0257	6.31	1.60	129.9 ± 4.7
1130	11.737	0.0189	5.0718	0.0201	6.53	11.0	134.1 ± 1.8
1180	8.6838	0.0089	5.0614	0.0179	6.42	39.4	132.0 ± 1.7
1230	8.0289	0.0067	4.7931	0.0173	6.41	19.6	131.8 ± 1.5
1300	9.4648	0.0115	4.6454	0.0179	6.42	14.5	131.9 ± 1.8
1400	9.5503	0.0122	5.2526	0.0183	6.35	5.54	130.7 ± 1.9
XM31-2 hornblende, W = 0.301 g, J = 0.011716, TGA = 146.7 ± 2.6Ma, t_P = 141.9 ± 1.2 Ma (7–12 steps, 94.9% released ^{39}Ar), t_i = 142.0 ± 24 Ma, initial $^{40}Ar/^{36}Ar$ = 256 ± 85, MSWD = 5.8							
500	47.850	0.1045	34.780	0.0926	20.0	0.69	380.0 ± 14
600	101.56	0.2813	29.627	0.1258	21.0	0.41	397.0 ± 31
700	82.295	0.2499	18.704	0.0920	9.93	0.44	199.0 ± 22
800	59.788	0.1706	10.391	0.0616	10.2	0.7	203.0 ± 21
900	39.218	0.1018	7.1505	0.0453	9.69	1.34	194.0 ± 11
1000	26.018	0.0611	4.8161	0.0327	8.34	1.53	168.3 ± 5.2
1100	11.875	0.0175	5.5051	0.0264	7.12	19.0	144.6 ± 2.5
1150	10.482	0.0129	4.6321	0.0227	7.02	20.0	142.6 ± 2.0
1200	8.7757	0.0075	4.7119	0.0200	6.93	26.1	140.8 ± 1.8
1250	8.8575	0.0076	4.7152	0.0197	6.95	12.8	141.3 ± 1.6
1300	9.2105	0.0088	5.2152	0.0205	6.99	16.5	142.1 ± 1.7
1400	11.266	0.0188	14.540	0.0289	6.81	0.64	138.4 ± 5.1
XM52-1 biotite, W = 0.050 g, J = 0.011927, TGA = 134.0 ± 1.7 Ma, t_P = 127.1 ± 0.7 Ma (5–12 steps, 88.2% released ^{39}Ar), t_i = 126.4 ± 0.9 Ma, initial $^{40}Ar/^{36}Ar$ = 308 ± 15, MSWD = 1.3							
400	23.509	0.0441	21.943	0.0836	12.2	0.65	245.9 ± 7.0
500	23.994	0.0394	2.4256	0.0325	12.5	1.31	251.2 ± 4.6
600	22.740	0.0482	1.2039	0.0288	8.60	3.96	176.1 ± 3.5
700	17.548	0.0307	0.2562	0.0227	8.48	5.45	173.9 ± 2.8
800	8.2542	0.0071	0.3224	0.0158	6.17	18.0	128.1 ± 1.8
900	6.7776	0.0021	0.0668	0.0141	6.16	13.6	127.9 ± 1.4
950	6.5992	0.0018	0.1373	0.0144	6.06	4.88	125.9 ± 1.4
1000	6.9130	0.0025	0.1829	0.0150	6.19	5.66	128.4 ± 1.5
1100	6.5966	0.0016	0.0533	0.0146	6.11	7.39	127.1 ± 1.4
1200	6.3648	0.0011	0.0494	0.0145	6.03	12.7	125.3 ± 1.6
1300	6.3939	0.0010	0.0195	0.0139	6.10	24.6	126.7 ± 1.4
1400	6.9713	0.0029	0.6236	0.0156	6.17	1.80	128.0 ± 1.6
XM52-1 hornblende, W = 0.295 g, J = 0.011716, TGA = 143.8 ± 3.3 Ma, t_P = 128.3 ± 0.9 Ma (7–11 steps, 98.4% released ^{39}Ar), t_i = 123.9 ± 1.4 Ma, initial $^{40}Ar/^{36}Ar$ = 298.8 ± 3.4, MSWD = 1.5							

Table 2 (*continued*)

T(°C)	$(^{40}Ar/^{39}Ar)_m$	$(^{36}Ar/^{39}Ar)_m$	$(^{37}Ar/^{39}Ar)_m$	$(^{38}Ar/^{39}Ar)_m$	$^{40}Ar^*/^{39}Ar$	^{39}Ar/%	Age ± 1σ/Ma
600	165.57	0.5405	6.6783	0.1248	6.34	0.18	129.0 ± 49
700	65.009	0.2077	14.463	0.0943	4.71	0.08	97.0 ± 48
800	47.673	0.1430	9.9601	0.0549	6.15	0.14	126.0 ± 32
900	50.037	0.1490	6.3672	0.0547	6.50	0.23	132.0 ± 20
1000	21.966	0.0597	5.7731	0.0311	4.75	0.51	97.7 ± 7.5
1100	23.141	0.0673	9.5396	0.0365	3.94	0.42	81.5 ± 7.7
1200	7.7275	0.0060	3.8779	0.0220	6.24	16.9	127.2 ± 1.5
1250	7.1667	0.0041	3.8637	0.0214	6.25	21.8	127.4 ± 1.5
1300	7.1052	0.0037	3.7344	0.0211	6.28	38.4	128.1 ± 1.4
1350	7.5234	0.0050	4.1010	0.0219	6.34	16.8	129.3 ± 1.4
1400	7.8581	0.0062	5.0254	0.0215	6.40	4.58	130.4 ± 2.0
XM52-2 hornblende, W = 0.295 g, J = 0.011828, TGA = 124.4 ± 1.4 Ma, t_P = 127.0 ± 0.8 Ma (7–12 steps, 98.0% released ^{39}Ar), t_i = 121.6 ± 1.2 Ma, initial $^{40}Ar/^{36}Ar$ = 289.3 ± 5.3, MSWD = 0.5							
500	50.337	0.1490	10.376	0.0677	7.09	0.27	145.0 ± 26
600	148.42	0.4929	25.197	0.1390	4.65	0.18	97.0 ± 44
700	74.611	0.2347	7.5371	0.0683	5.82	0.27	120.0 ± 23
800	78.423	0.2305	5.4684	0.0702	10.7	0.28	216.0 ± 28
900	51.310	0.1293	3.1053	0.0394	13.4	0.39	265.0 ± 18
1000	30.465	0.0797	3.5073	0.0320	7.17	0.59	147.0 ± 12
1080	16.455	0.0365	4.7609	0.0266	6.01	1.91	123.9 ± 4.5
1130	8.0518	0.0074	4.1559	0.0216	6.16	12.2	126.9 ± 1.4
1180	7.3645	0.0052	4.0683	0.0209	6.13	26.7	126.2 ± 1.4
1230	6.8998	0.0035	4.0374	0.0206	6.16	29.9	126.8 ± 1.4
1300	7.3633	0.0049	4.3082	0.0212	6.23	24.5	128.2 ± 1.4
1400	7.7774	0.0066	4.5356	0.0218	6.17	2.87	127.1 ± 1.6
XM101-2 biotite, W = 0.051 g, J = 0.011794, TGA = 122.1 ± 1.5 Ma, t_P = 122.5 ± 0.6 Ma (6–12 steps, 93.4% released ^{39}Ar), t_i = 123.0 ± 0.9 Ma, initial $^{40}Ar/^{36}Ar$ = 279 ± 14, MSWD = 0.6							
500	21.3472	0.0533	16.4178	0.0915	6.86	0.03	140.0 ± 16
600	17.6640	0.0558	13.9900	0.0754	2.17	0.09	45.7 ± 8.2
700	13.7075	0.0326	3.4632	0.0332	4.32	0.38	89.6 ± 6.8
800	12.4509	0.0195	1.9236	0.0334	6.82	4.01	139.6 ± 2.3
900	12.5083	0.0302	1.5275	0.0242	3.70	2.12	77.1 ± 2.9
1000	8.3304	0.0084	0.2106	0.0157	5.86	9.90	120.5 ± 1.7
1060	6.3396	0.0014	0.1176	0.0143	5.93	16.4	121.9 ± 1.3
1140	6.2692	0.0009	0.1283	0.0142	6.01	11.5	123.5 ± 1.3
1220	6.3433	0.0011	0.1142	0.0140	6.02	16.0	123.8 ± 1.6
1300	6.1756	0.0007	0.0721	0.0139	5.98	18.4	122.9 ± 1.3
1360	6.1605	0.0007	0.0464	0.0137	5.95	18.0	122.3 ± 1.3
1450	6.3085	0.0013	0.2632	0.0141	5.93	3.22	121.9 ± 1.4
XM102-2 hornblende, W = 0.051 g, J = 0.011685, TGA = 119.6 ± 1.5 Ma, t_P = 120.7 ± 0.7 Ma (6–12 steps, 97.9% released ^{39}Ar), t_i = 121.0 ± 0.8 Ma, initial $^{40}Ar/^{36}Ar$ = 274.4 ± 17, MSWD = 1.3							
500	16.961	0.0251	14.470	0.0726	10.7	0.14	212.0 ± 22
600	19.607	0.0548	17.829	0.0895	4.75	0.07	97.0 ± 28
700	13.168	0.0366	7.1159	0.0389	2.88	0.25	59.7 ± 8.6
800	9.3933	0.0261	7.8022	0.0456	2.24	0.30	47.0 ± 15
900	11.791	0.0278	1.3245	0.0228	3.68	1.36	76.0 ± 4.0
1000	7.5697	0.0060	0.0944	0.0150	5.81	6.93	118.5 ± 1.6
1070	6.1378	0.0009	0.1112	0.0139	5.89	22.7	120.0 ± 1.7
1140	6.1169	0.0008	0.1594	0.0142	5.89	5.78	120.0 ± 1.8
1220	6.2123	0.0009	0.1914	0.0140	5.97	9.50	121.6 ± 1.3
1300	6.1104	0.0006	0.0434	0.0138	5.92	23.1	120.7 ± 1.2
1400	6.0290	0.0004	0.0393	0.0136	5.91	28.2	120.6 ± 1.2
1450	6.4555	0.0016	0.4468	0.0164	6.02	0.00	122.7 ± 1.6

the XMSZ as constrained from the obtained U–Pb zircon LA-ICPMS ages for the undeformed granite dikes.

The hornblende ages from the XMSZ are synchronous with intrusion times of the earlier stage, deformed plutons (Xu et al., 2007; Wang et al., 2007). This indicates that the ductile shearing along the XMSZ is associated with the earliest magmatism in the NDD. Previous work also proposed that the onset of extensional tectonism in the NDD was prior to 145 Ma (e.g. Wu et al., 2007; Zhu et al., 2010a) and the minimum age of deformed intrusions is 132 Ma (Xu et al., 2007). This is consistent with our new dating results and we suggest that ductile shearing along the XMSZ occurred from 145 Ma to 132 Ma.

We also note that our ^{40}Ar–^{39}Ar ages for the XMSZ are similar to the ^{40}Ar–^{39}Ar ages for the WSSZ (126 Ma biotite and 130 Ma muscovite) obtained by Ratschbacher et al. (2000) as well as the zircon margin ages from deformed intrusions and migmatited gneisses in the interior of the NDD (137–143 Ma) obtained by Wang et al. (2007), Wu et al. (2007) and Xu et al. (2007). We therefore suggest that the XMSZ, the WSSZ, and the interior of the NDD were all involved in the same deformation event of the earliest Early Cretaceous.

5.2. The East Dabie Detachment zone

As described earlier, the XMSZ is curved and structures along it exhibit systematically variable kinematics from sinistral motion with minor normal component in the east segment to sinistral transtension in the west segment (Fig. 4). There are two possible

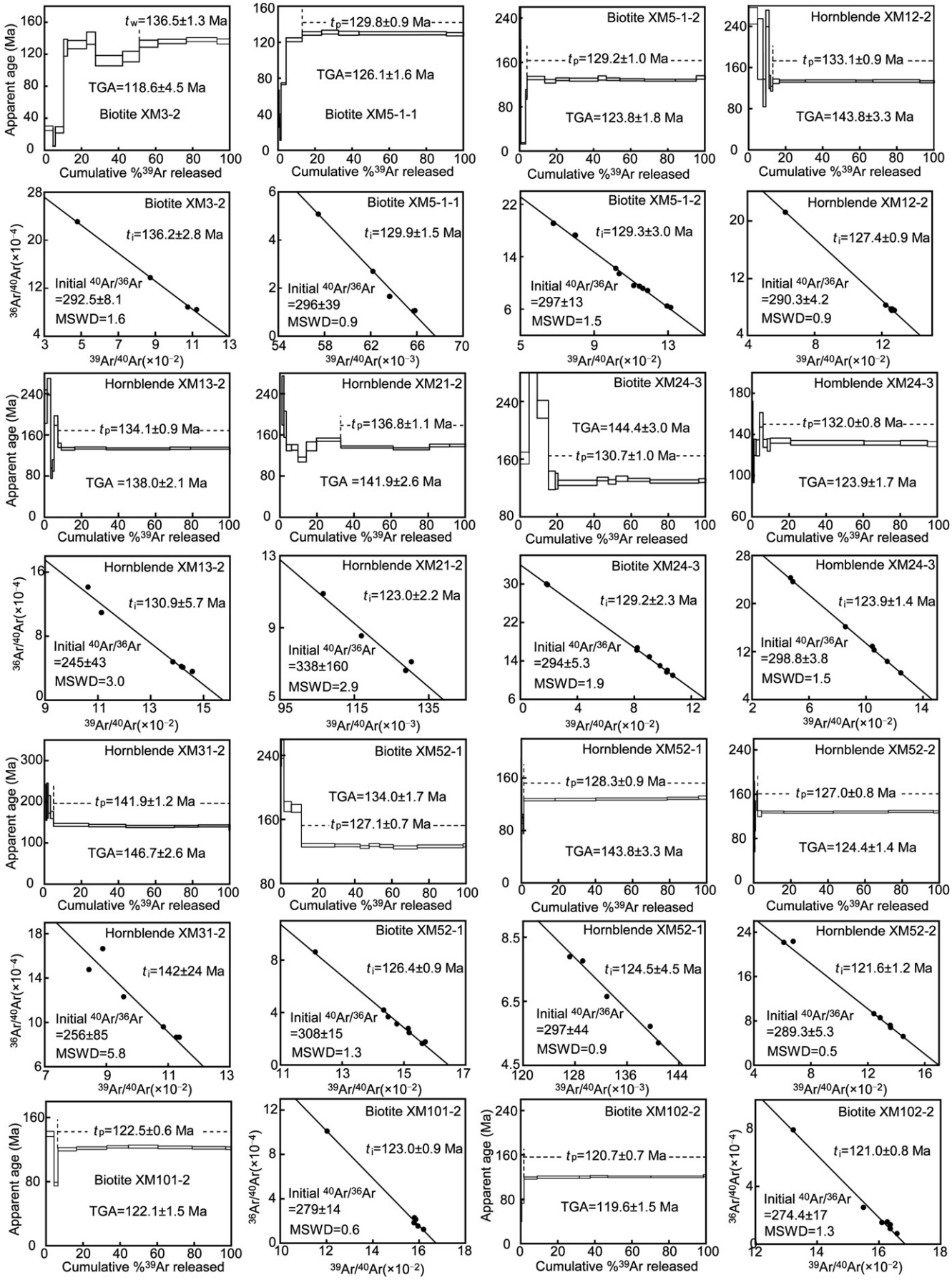

Fig. 7. Age spectra and inverse isochron plots for hornblende and biotite samples from the Xiaotian-Mozitan shear zone. TGA, total gas age; t_p, plateau age; t_i, inverse isochron age; t_w, weighted mean age.

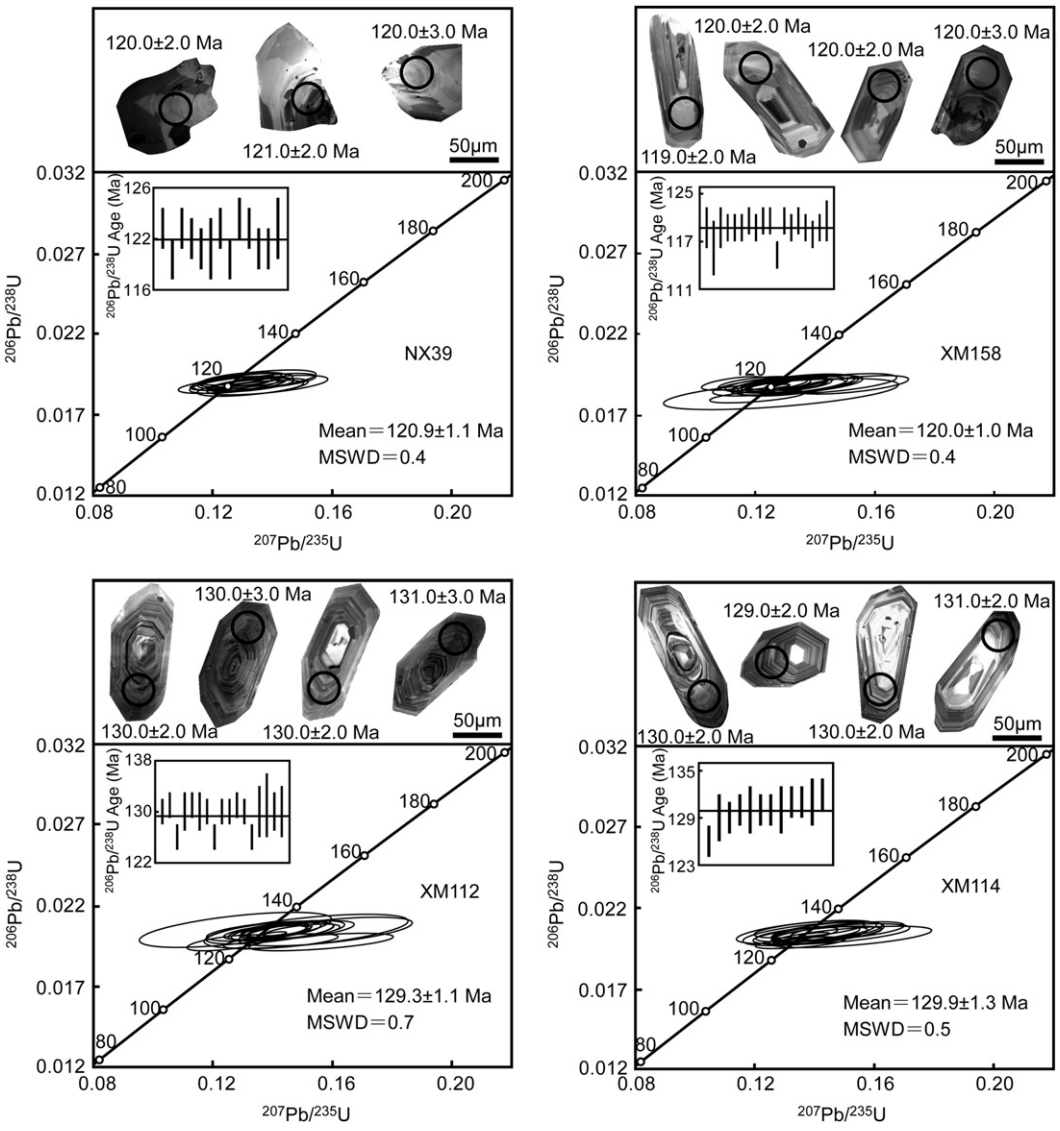

Fig. 8. Representative cathodoluminescence (CL) images of the dated zircons and LA-ICPMS U–Pb zircon Concordia diagram of the undeformed granite dikes in the Xiaotian-Mozitan shear zone. Inset shows distribution of $^{206}Pb/^{238}U$ age bars. Error bars are 1σ. Solid horizontal bar are the weighted ages.

explanations for the curvature of the shear zone. One is that the curvature is primary – the XMSZ was originally a curved zone. The other explanation is that the curvature is due to modification by subsequent doming. Structural geometry within the XMSZ and the variation in the uplift history across the area support the second explanation. The rather smooth variation in kinematics along the zone as the zone curves can be best explained by the superposition of a deformation following the formation of the ductile fabrics. The middle segment of the XMSZ changes its strikes from WNW–ESE to NW–SE or even NNW–SSE locally. If the shear zone boundaries were curved originally, the structures in the curved segment should show an enhanced thrusting component (Lin and Jiang, 2001). The curved segment shows sinistral motion with a minor normal component instead (Fig. 1), suggesting that the XMSZ was curved after it was formed. A local shear belt with ESE-plunging stretching lineation on SSW-dipping mylonitic foliation was found in the east segment dominated by NNE-dipping foliation with a sinistral shear sense. The local shear zone shows a top-to-NW or WNW shear sense rather than a sinistral sense which would be expected if the current orientation of the shear zone was not a modified one. In fact, the kinematics of the XMSZ becomes quite uniform once the curvature of the zone boundaries is removed. The NDD becomes wider to the west, and the UHP slab, originally overlying on the NDD (Hacker et al., 2000; Ratschbacher et al., 2000; Faure et al., 2003), is only preserved in the southeast of the NDD (Fig. 1). Therefore there is more uplift for the western part of the NDD. Previous data on erosion depth (Yang et al., 2000) for the Early Cretaceous plutons in the NDD also suggests that doming was more enhanced to west. The inhomogeneous doming seems to be compatible with the presently apparent "transtension" kinematics in the west and sinistral sense in the east along the XMSZ. In this case, however, one expects older cooling ages for the west segment due to its faster and earlier uplifting. But the opposite is observed – the obtained $^{40}Ar–^{39}Ar$ ages from the western segment are significantly younger than those of the same minerals from the eastern segment (Figs. 1 and 7). This problem is resolved if the present geometry and kinematics of the XMSZ are due to the overprinting by doming. The east segment of the XMSZ is close to the centre of the Yuexi dome and this can explain the present shallow-plunging lineations on the NNE-dipping mylonitic

Table 3
Detailed LA-ICPMS zircon U–Pb analytical data.

Analysis	Content ($\times 10^{-6}$)			$^{207}Pb/^{206}Pb$		$^{207}Pb/^{235}U$		$^{206}Pb/^{238}U$		$^{208}Pb/^{232}Th$		$^{207}Pb/^{206}Pb$		$^{207}Pb/^{235}U$		$^{206}Pb/^{238}U$		$^{208}Pb/^{232}Th$	
	U^{238}	Th^{232}	Th/U	Ratio	±1σ	Ratio	±1σ	Ratio	±1σ	Ratio	±1σ	Age	±1σ	Age	±1σ	Age	±1σ	Age	±1σ
NX39-1	98.5	139	1.41	0.0499	0.0041	0.1310	0.0104	0.0190	0.0003	0.0057	0.0001	190	148	125	9	122	2	115	3
NX39-2	81.5	111	1.36	0.0519	0.0049	0.1335	0.0122	0.0187	0.0004	0.0058	0.0002	280	171	127	11	119	2	116	3
NX39-3	136	163	1.20	0.0493	0.0034	0.1298	0.0088	0.0191	0.0003	0.0058	0.0001	160	123	124	8	122	2	116	3
NX39-4	108	130	1.20	0.0484	0.0036	0.1263	0.0090	0.0189	0.0003	0.0057	0.0001	121	131	121	8	121	2	115	3
NX39-5	96.7	147	1.52	0.0484	0.0044	0.1255	0.0111	0.0188	0.0003	0.0061	0.0002	118	163	120	10	120	2	124	3
NX39-6	72.9	96.7	1.33	0.0534	0.0053	0.1384	0.0133	0.0188	0.0004	0.0067	0.0002	344	179	132	12	120	3	135	4
NX39-7	105	136	1.30	0.0531	0.0039	0.1393	0.0101	0.0190	0.0003	0.0055	0.0001	332	135	132	9	122	2	112	3
NX39-8	122	140	1.15	0.0527	0.0040	0.1355	0.0099	0.0186	0.0003	0.0019	0.0002	316	136	129	9	119	2	38	4
NX39-9	156	174	1.12	0.0485	0.0031	0.1283	0.0079	0.0192	0.0003	0.0058	0.0001	123	112	123	7	123	2	118	3
NX39-10	91.9	132	1.44	0.0493	0.0037	0.1300	0.0096	0.0191	0.0003	0.0059	0.0001	162	136	124	9	122	2	118	3
NX39-11	89.1	119	1.34	0.0495	0.0042	0.1284	0.0107	0.0188	0.0003	0.0060	0.0002	172	153	123	10	120	2	121	3
NX39-12	105	131	1.25	0.0512	0.0037	0.1330	0.0094	0.0188	0.0003	0.0061	0.0001	251	133	127	8	120	2	123	3
NX39-13	105	164	1.56	0.0509	0.0053	0.1340	0.0136	0.0191	0.0004	0.0059	0.0002	238	187	128	12	122	3	118	4
XM112-1	295	263	0.89	0.0501	0.0029	0.1410	0.0078	0.0204	0.0003	0.0065	0.0002	201	103	134	7	130	2	131	3
XM112-2	254	217	0.85	0.0500	0.0028	0.1413	0.0078	0.0205	0.0003	0.0063	0.0002	195	102	134	7	131	2	127	3
XM112-3	247	207	0.84	0.0461	0.0035	0.1252	0.0092	0.0197	0.0003	0.0064	0.0002	991	167	120	8	126	2	130	5
XM112-4	195	134	0.69	0.0495	0.0051	0.1391	0.0141	0.0204	0.0005	0.0065	0.0003	171	184	132	13	130	3	132	6
XM112-5	317	309	0.97	0.0507	0.0031	0.1433	0.0086	0.0205	0.0003	0.0066	0.0002	226	111	136	8	131	2	133	3
XM112-6	309	220	0.71	0.0513	0.0047	0.1447	0.0129	0.0205	0.0004	0.0066	0.0003	255	163	137	11	130	3	132	5
XM112-7	281	227	0.81	0.0509	0.0041	0.1434	0.0113	0.0204	0.0004	0.0067	0.0002	237	144	136	10	130	2	136	5
XM112-8	267	240	0.90	0.0523	0.0047	0.1429	0.0126	0.0198	0.0003	0.0062	0.0001	300	205	136	11	126	2	125	1
XM112-9	308	255	0.83	0.0503	0.0023	0.1416	0.0063	0.0204	0.0002	0.0064	0.0001	207	82	134	6	1301	2	129	3
XM112-10	236	186	0.79	0.0531	0.0031	0.1497	0.0085	0.0204	0.0003	0.0065	0.0002	334	103	142	7	130	2	130	3
XM112-11	244	207	0.85	0.0528	0.0043	0.1493	0.0119	0.0205	0.0004	0.0064	0.0002	321	146	141	10	131	2	128	4
XM112-12	178	127	0.71	0.0490	0.0034	0.1378	0.0093	0.0204	0.0003	0.0064	0.0002	148	123	131	8	130	2	129	4
XM112-13	164	118	0.72	0.0574	0.0060	0.1563	0.0160	0.0198	0.0004	0.0061	0.0001	506	236	147	14	126	2	124	2
XM112-14	175	119	0.68	0.0560	0.0070	0.1576	0.0193	0.0204	0.0006	0.0062	0.0004	452	221	149	17	130	4	126	8
XM112-15	190	140	0.74	0.0487	0.0046	0.1370	0.0127	0.0204	0.0004	0.0066	0.0003	131	169	130	11	130	3	133	5
XM112-16	198	119	0.60	0.0537	0.0082	0.1512	0.0226	0.0204	0.0007	0.0062	0.0005	359	275	143	20	130	4	124	10
XM114-1	197	212	1.08	0.0546	0.0061	0.1441	0.0158	0.0192	0.0005	0.0061	0.0003	395	202	137	14	122	3	123	5
XM114-2	94.2	85.9	0.91	0.0574	0.0054	0.1531	0.0141	0.0193	0.0004	0.0063	0.0002	508	167	145	12	123	3	127	5
XM114-3	322	365	1.13	0.0501	0.0035	0.1335	0.0090	0.0193	0.0003	0.0064	0.0002	198	123	127	8	123	2	128	3
XM114-4	196	170	0.87	0.0518	0.0049	0.1373	0.0127	0.0192	0.0004	0.0059	0.0002	278	172	131	11	123	2	119	5
XM114-5	225	225	1.00	0.0503	0.0040	0.1352	0.0105	0.0195	0.0003	0.0063	0.0002	208	143	129	9	124	2	126	4
XM114-6	165	155	0.94	0.0495	0.0047	0.1326	0.0122	0.0194	0.0004	0.0064	0.0002	170	169	126	11	124	3	128	5
XM114-7	281	318	1.13	0.0599	0.0049	0.1604	0.0126	0.0194	0.0004	0.0063	0.0002	601	137	151	11	124	2	126	4
XM114-8	148	144	0.97	0.0574	0.0074	0.1549	0.0196	0.0196	0.0006	0.0067	0.0003	507	227	146	17	125	4	135	7
XM114-9	394	511	1.30	0.0495	0.0037	0.1353	0.0099	0.0198	0.0002	0.0063	0.0001	172	168	129	9	126	2	126	1
XM114-10	224	206	0.92	0.0546	0.0066	0.1520	0.0180	0.0202	0.0004	0.0063	0.0001	395	274	144	16	129	3	127	2
XM114-11	229	230	1.00	0.0507	0.0039	0.1417	0.0107	0.0203	0.0003	0.0064	0.0002	225	140	135	9	129	2	128	4
XM114-12	185	136	0.74	0.0513	0.0044	0.1441	0.0122	0.0204	0.0003	0.0064	0.0001	254	197	137	11	130	2	129	1
XM114-13	172	160	0.93	0.0519	0.0062	0.1457	0.0173	0.0204	0.0004	0.0064	0.0001	281	272	138	15	130	3	129	2
XM114-14	330	349	1.06	0.0487	0.0026	0.1369	0.0072	0.0204	0.0003	0.0067	0.0001	131	96	130	6	130	2	135	3
XM114-15	238	250	1.05	0.0491	0.0042	0.1378	0.0115	0.0204	0.0003	0.0064	0.0001	152	191	131	10	130	2	130	2
XM114-16	246	211	0.86	0.0497	0.0057	0.1397	0.0156	0.0204	0.0005	0.0059	0.0003	181	205	133	14	130	3	120	6
XM114-17	152	148	0.97	0.0533	0.0045	0.1510	0.0126	0.0206	0.0004	0.0070	0.0002	340	155	143	11	131	2	141	4
XM114-18	210	219	1.04	0.0510	0.0044	0.1442	0.0123	0.0205	0.0004	0.0064	0.0002	239	157	137	11	131	2	129	4
XM114-19	156	145	0.93	0.0486	0.0056	0.1374	0.0155	0.0205	0.0005	0.0063	0.0003	130	208	131	14	131	3	127	5
XM114-20	139	128	0.92	0.0485	0.0044	0.1383	0.0122	0.0207	0.0004	0.0064	0.0002	125	165	131	11	132	2	128	4
XM158-1	87.7	90.6	1.03	0.0483	0.0050	0.1248	0.0125	0.0187	0.0004	0.0056	0.0002	115	184	119	11	120	3	113	4
XM158-2	77.9	85.6	1.10	0.0511	0.0105	0.1286	0.0259	0.0183	0.0006	0.0058	0.0002	245	383	123	23	117	4	116	5
XM158-3	61.2	89.9	1.47	0.0510	0.0054	0.1326	0.0138	0.0189	0.0004	0.0059	0.0002	243	194	126	12	120	3	118	4
XM158-4	107	121	1.13	0.0476	0.0036	0.1237	0.0092	0.0188	0.0003	0.0058	0.0002	81	133	118	8	120	2	116	3
XM158-5	115	171	1.49	0.0484	0.0033	0.1256	0.0085	0.0188	0.0003	0.0058	0.0001	119	123	120	8	120	2	116	2
XM158-6	175	210	1.20	0.0514	0.0028	0.1338	0.0070	0.0189	0.0003	0.0058	0.0001	260	95	127	6	120	2	117	2

Table 3 (*continued*)

Analysis	Content ($\times 10^{-6}$)			$^{207}Pb/^{206}Pb$		$^{207}Pb/^{235}U$		$^{206}Pb/^{238}U$		$^{208}Pb/^{232}Th$		$^{207}Pb/^{206}Pb$		$^{207}Pb/^{235}U$		$^{206}Pb/^{238}U$		$^{208}Pb/^{232}Th$	
	U^{238}	Th^{232}	Th/U	Ratio	±1σ	Ratio	±1σ	Ratio	±1σ	Ratio	±1σ	Age	±1σ	Age	±1σ	Age	±1σ	Age	±1σ
XM158-7	146	170	1.16	0.0460	0.0032	0.1199	0.0082	0.0189	0.0003	0.0058	0.0001	−3	118	115	7	121	2	116	3
XM158-8	94.9	112	1.18	0.0517	0.0044	0.1342	0.0110	0.0188	0.0004	0.0058	0.0002	274	152	128	10	120	2	118	3
XM158-9	123	125	1.02	0.0497	0.0038	0.1296	0.0095	0.0189	0.0003	0.0065	0.0002	181	135	124	9	121	2	130	3
XM158-10	201	215	1.07	0.0433	0.0029	0.1131	0.0073	0.0189	0.0003	0.0059	0.0001	−105	115	109	7	121	2	118	3
XM158-11	192	278	1.45	0.0484	0.0043	0.1206	0.0105	0.0181	0.0003	0.0057	0.0001	117	200	116	10	116	2	116	1
XM158-12	117	132	1.13	0.0500	0.0033	0.1305	0.0085	0.0189	0.0003	0.0056	0.0001	193	122	125	8	121	2	113	3
XM158-13	87.3	109	1.25	0.0586	0.0050	0.1521	0.0126	0.0188	0.0004	0.0062	0.0002	552	147	144	11	120	2	124	4
XM158-14	208	202	0.97	0.0538	0.0042	0.1400	0.0105	0.0189	0.0004	0.0060	0.0002	363	136	133	9	121	2	121	4
XM158-15	96.7	110	1.14	0.0522	0.0049	0.1358	0.0124	0.0189	0.0004	0.0057	0.0002	296	168	129	11	120	2	115	4
XM158-16	99.7	126	1.26	0.0514	0.0046	0.1325	0.0117	0.0187	0.0004	0.0060	0.0002	258	164	126	10	119	2	121	3
XM158-17	133	154	1.16	0.0501	0.0041	0.1299	0.0104	0.0188	0.0003	0.0059	0.0002	200	151	124	9	120	2	120	3
XM158-18	107	126	1.18	0.0558	0.0057	0.1454	0.0144	0.0189	0.0004	0.0058	0.0002	444	184	138	13	121	3	117	4

foliation. The west segment is farther away from the centre of a dome (the Luotian dome) and therefore has oblique lineation because of differential rotation away from a dome centre. The curved middle segment of the XMSZ is a result of the differential rotation and warping between the eastern and western segments during the doming. The folded patterns of the WSSZ along its strike also resulted from the same mechanism (Fig. 1).

Field observations, quartz c-axis patterns, and microstructures show that the XMSZ and the WSSZ both have a top-to-WNW or NW shear sense and overprint the gneisses of the NDD. In fact, if the doming effect discussed above is removed, both shear zones naturally merge into a single zone. The two shear zones also have similar Early Cretaceous $^{40}Ar-^{39}Ar$ ages and deformation temperatures. The interior of the NDD, the footwall of the XMSZ and the WSSZ, also exhibit widespread, top-to-NW or WNW Early Cretaceous ductile shearing. The dome shape of the NDD is well defined by the gradual variation of the gneissositic foliation inside the NDD (Fig. 1c). Combining all, it is most likely that the XMSZ and the WSSZ were originally a single, more flat-lying detachment shear zone with a top-to-NW or WNW shear sense before the doming of the NDD (Fig. 9). We call this zone the East Dabie Detachment zone (EDDZ). The interior of the NDD represents the footwall of the EDDZ whereas the UHP slab to the southeast and the NH unit to the north belong to its hanging wall.

Since deformation of the XMSZ and the WSSZ occurred at temperatures of 600–650 °C, taking the typical geothermal gradient of 35–40 °C/km for an extension setting, the original, more flat-lying EDDZ was at depths of 15–18 km. By using the Al-in-hornblende geobarometer for the Early Cretaceous plutons and orthogneisses inside the NDD, Yang et al. (2000) and Ratschbacher et al. (2000) suggested an average exhumation of 18 km with maximum of 30 km for the NDD since the Early Cretaceous. These data suggest that the EDDZ was at a middle crustal level at the time of Early Cretaceous before exhumed and partly eroded during doming of the NDD.

5.3. Formation process and mechanism of the NDD

Ductile lateral flow of thickened orogenic crust has been widely reported (e.g. Meissner and Mooney, 1998; Liu, 2001; Rey et al., 2001; Vanderhaeghe and Teyssier, 2001; Klepeis et al., 2004). In a thickened orogenic belt, a flat-lying to gently-dipping detachment shear zone can develop between overlying brittle crust and underlying ductile crust at the later stage of or after tectonic convergence (see discussion in Williams and Jiang, 2005, and references therein). This is the same with the EDDZ (Fig. 9). The lower crustal flow underneath the detachment shear zone was accompanied by widespread migmatization and ductile deformation in the interior of the NDD. The uniform top-to-NW or WNW shear sense of the EDDZ suggests an increase in flow velocity with depth (Fig. 9a). The shearing along the EDDZ overlapped with the earlier stage of the magmatism but terminated before widespread magmatic intrusion took place. The resultant buoyancy increase of the crust might account for the doming of the NDD and the associated distortion of the EDDZ (Fig. 9b).

In this work, hornblende and biotite ages from the same sample of XM24-3 in the XMSZ show a difference of only 1.3 Ma (Fig. 7). Based on closure temperatures of 550 °C for hornblende and 300 °C for biotite, it can be concluded that the XMSZ experienced a fast cooling event during 132–130 Ma mostly associated with the doming of the NDD. This fast cooling and uplifting of the XMSZ were roughly synchronous with the fast crustal thinning suggested by the switch of adakitic granite intrusion to non-adakitic granite intrusion in the NDD between 132 Ma and 129 Ma (Wang et al., 2007; Xu et al., 2007; Huang et al., 2008). Therefore, fast uplifting

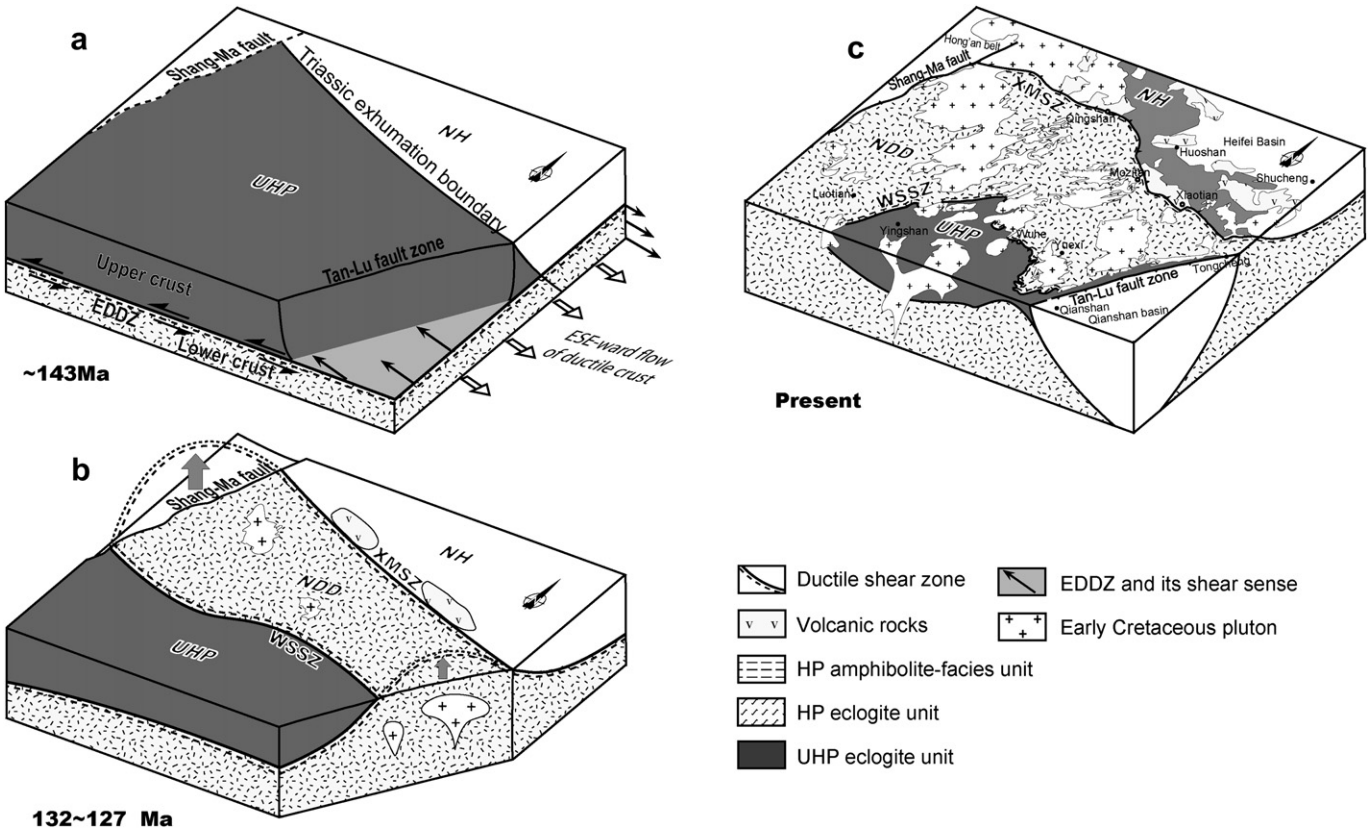

Fig. 9. Block diagrams for orogen-parallel extension of the ductile lithosphere; a: An earlier stage with ESE-ward flow of ductile crust and development of a flat-lying detachment shear zone (EDDZ) in the earliest Early Cretaceous; b: A later stage with the doming and passive warping of the detachment shear zone in the middle Early Cretaceous associated with large-scale intrusion; c: Present stage.

of the NDD occurred at about 132 Ma. Hornblende and biotite ages from the same samples of XM52-1 exhibit a difference of 1.2 Ma, which indicates that fast uplifting of the NDD may have lasted to 127 Ma. The dating results for metamorphic rocks inside of the NDD by Ratschbacher et al. (2000) and Hu et al. (2006) demonstrated that the process of the cooling and uplifting of the NDD had slowed down since 120 Ma when magmatism was much weaker (Zhao et al., 2007). This is consistent with our new dating results and we suggest that the fast uplifting of the NDD might have terminated at about 120 Ma.

As mentioned before, deep subduction and UHP-HP rocks exhumation to shallow crustal level occurred before the Early Jurassic (e.g. Hacker et al. 2000; Li et al., 2005), but orogen-scale extension did not happen until the earliest Early Cretaceous. We note that the Early Cretaceous extension in eastern Dabie and the development of the NDD are synchronous with the widespread extension related to lithospheric thinning in East China (e.g., Gao et al., 2002; Xu et al., 2004; Wu et al., 2005; Zhang et al., 2005; Zhu et al., 2010a,b). This suggests that development of the NDD was under the same geodynamic setting as the eastern NCB. Many metamorphic core complexes were also developed in the eastern NCB during Early Cretaceous (Zhang et al., 2000; Darby et al., 2004; Yang et al., 2007; Lin et al., 2008). As mentioned by Liu et al. (2005a,b), almost all of the detachment shear zones in these core complexes show a top-to-NW or WNW shear sense. The uniform shear sense suggests a uniform flow direction of the ductile lithosphere that reflects the intraplate deformation of the lithosphere (Bird, 1991; Beaumont et al., 2001; Williams and Jiang, 2005; Harris, 2007) rather than due to gravitational collapse (e.g. Dewey, 1988; Rey et al., 2001; Vanderhaeghe and Teyssier, 2001; Al-Zoubi and TenBrink, 2002). As proposed by many researchers (e.g. Ratschbacher et al., 2000; Wu et al., 2005), orthogonal, high-angle subduction of the Pacific plate might be responsible for the continental-scale, extensional regime in East China. East China lithospheric thinning was developed under the setting of the Pacific plate roll-back.

6. Conclusions

The XMSZ and the WSSZ were a single, connected, flat-lying detachment shear zone which we called the East Dabie Detachment Zone between the upper brittle crust and the lower ductile crust in the earliest Early Cretaceous in the Dabie Orogenic belt.

The kinematics in the XMSZ and the WSSZ and the interior of the NDD suggest that the EDDZ had a uniform top-to-NW or WNW sense of shear. This in turn suggests orogen-parallel extension of the ductile lithosphere in the east Dabie Orogenic belt in the Early Cretaceous.

The uniform shearing along the EDDZ probably started before 143 Ma and terminated at 132 Ma. After 132 Ma, fast crustal thinning and doming of the NDD were associated with large-scale magmatism. Doming of the NDD modified the EDDZ into an antiformal shape. Subsequent erosional removal of the hanging wall in the broad hinge area of this dome led to the separation of the EDDZ into two separate zones as we observe today.

Many metamorphic core complexes were also developed in eastern NCB during Early Cretaceous (Yang et al., 2007; Lin et al., 2008) almost all of which show top-to-NW or WNW shear sense. Such a widespread uniform shear sense suggests a uniform flow direction of the ductile lithosphere in east China that must have

been due to intraplate deformation of the lithosphere (Bird, 1991; Beaumont et al., 2001; Williams and Jiang, 2005; Harris, 2007).

Acknowledgements

This study was funded by the National Natural Science Foundation of China (grants number 40602025, 90714004, and 40828001) and Canada's NSERC discovery grant to DJ. We gratefully acknowledge the support and advice on the $^{40}Ar-^{39}Ar$ analyses from Mr. Chen Wen from the Ar–Ar Laboratory, Institute of Geology, Chinese Academy of Geological Sciences and the U–Pb zircon LA-ICPMS from Dr. Liu Xiaoming from the State Key Laboratory of Continental Dynamics, Department of Geology, Northwest University, Xi'an. We give our sincerest thanks to Prof. Zheng Yadong and Dr. Zhang Jian for their constructive comments that improved the final version of the manuscript greatly. We feel highly honored to have this paper published in a special issue honoring Paul Williams. Paul visited Hefei University of Technology in 1986 and his lectures at Hefei inspired many geologists.

References

Altenberger, U., 2000. Ductile deformation of K-feldspar in dry eclogite facies shear zones in the Bergen Arcs, Norway. Tectonophysics 320, 107–121.

Al-Zoubi, A., TenBrink, U., 2002. Lower crustal flow and the role of shear in basin subsidence: an example from the Dead Sea basin. Earth and Planetary Science Letters 199 (1–2), 67–79.

Ames, L., Zhou, G.Z., Xiong, B.C., 1996. Geochronology and isotopic character of ultrahigh-pressure metamorphism with implications for collision of the Sino-Korean and Yangtze cratons, central China. Tectonics 15, 472–489.

Ayers, J.C., Dunkle, S., Gao, S., Miller, C.F., 2002. Constraints on timing of peak and retrograde metamorphism in the Dabie Shan ultrahigh-pressure metamorphic belt, east-central China, using U-Th-Pb dating of zircon and monazite. Chemical Geology 186, 315–331.

Beaumont, C., Jamieson, R.A., Nguyen, M.H., Lee, B., 2001. Himalayan tectonics explained by extrusion of a low-viscosity crustal channel coupled to focus surface denudation. Nature 414, 738–742.

Bird, P., 1991. Lateral extrusion of lower crust from under high topography, in the isostatic limit. Journal of Geophysical Research 96, 10275–10286.

Chen, F.K., Guo, J.H., Jiang, L.L., Siebel, W., Cong, B.L., Satir, M., 2003. Provenance of the Beihuaiyang lower-grade metamorphic zone of the Dabie ultrahigh-pressure collisional orogen, China: evidence from zircon ages. Journal of Asian Earth Sciences 22, 343–352.

Chen, N.S., Sun, M., You, Z.D., Malpas, J., 1998. Well preserved garnet growth zoning in granulite from the Dabie Mountains, central China. Journal of Metamorphic Geology 16, 213–222.

Darby, B.J., Davis, G.A., Zhang, X.H., 2004. The newly discovered Waziyu metamorphic core complex, Yiwulushan, Western Liaoning Province, Northeast China. Earth Science Frontiers 11, 145–155.

Dewey, J.F., 1988. Extensional collapse of orogens. Tectonics 7, 1123–1139.

Dodson, M.H., 1973. Closure temperature in cooling geochronological and petrological systems. Contributions to Mineralogy and Petrology 40, 259–274.

Eide, L., McWilliams, M.O., Liou, J.G., 1994. $^{40}Ar/^{39}Ar$ geochronologic constraints on the exhumation of HP-UHP metamorphic rocks in east-central China. Geology 22, 601–604.

Faure, M., Lin, W., Schärer, U., Shu, L.S., Sun, Y., Arnaud, N., 2003. Continental subduction and exhumation of UHP rocks. Structural and geochronological insights from the Dabieshan (East China). Lithos 70, 213–241.

Faure, M., Lin, W., Shu, L.L., Sun, Y., Schärer, U., 1999. Tectonics of the Dabieshan (eastern China) and possible exhumation mechanism of ultra-high pressure rocks. Terra Nova 11, 251–258.

Gao, S., Rudnick, R.L., Carlson, R.W., McDonough, W.F., Liu, Y.S., 2002. Re-Os evidence for replacement of ancient mantle lithosphere beneath the North China craton. Earth and Planetary Science Letters 198, 307–322.

Hacker, B.R., Ratschbacher, L., Webb, L., Dong, S.W., 1995. What brought them up? Exhumation of the Dabie Shan ultrahigh-pressure rocks. Geology 23 (8), 743–746.

Hacker, B.R., Ratschbacher, L., Webb, L., Ireland, T., Walker, D., Dong, S., 1998. U/Pb zircon ages constrain the architecture of the ultrahigh-pressure Qinling-Dabie Orogen, China. Earth and Planetary Science Letters 161, 215–230.

Hacker, B.R., Ratschbacher, L., Webb, L., McWilliams, M.O., Ireland, T., Calvert, A., Dong, S.W., Wenk, H.R., Chateigner, D., 2000. Exhumation of ultrahigh-pressure continental crust in east central China: Late Triassic-Early Jurassic tectonic unroofing. Journal of Geophysical Research 105 (B6), 13339–13364.

Hacker, B.R., Wang, Q.C., 1995. Ar/Ar geochronology of ultrahigh-pressure metamorphism in central China. Tectonics 14 (4), 994–1006.

Harris, N., 2007. Channel flow and the Himalayan-Tibetan orogen: a critical review. Journal of the Geological Society, London 164, 511–523.

Harrison, T.M., 1981. Diffusion of ^{40}Ar in hornblende. Contributions to Mineralogy and Petrology 78 (3), 324–331.

Hirth, G., Tullis, J., 1992. Dislocation creep regimes in quartz aggregates. Journal of structural geology 14 (2), 145–159.

Hu, S.B., Kohn, B.P., Raza, A., Wang, J.Y., Gleadow, A.J.W., 2006. Cretaceous and Cenozoic cooling history across the ultrahigh pressure Tongbai-Dabie belt, central China, from apatite fission-track thermochronology. Tectonophysics 420, 409–429.

Huang, F., Li, S.G., Dong, F., He, Y.S., Chen, F.K., 2008. High-Mg adakitic rocks in the Dabie orogen, central China: implications for foundering mechanism of lower continental crust. Chemical Geology 255, 1–13.

Jiang, L.L., Wu, W.P., Liu, Y.C., Li, H.M., 2003b. U-Pb zircon and Ar-Ar hornblende ages of the Susong complex of the southern Dabie orogen and their geological implication. Acta Petrologica Sinica 19 (3), 497–505.

Jiang, L.L., Wu, W.P., Liu, Y.C., Zhang, Y., Qian, C.C., 2003a. Progress of tectonic research on the (UHP) belt in the eastern Dabieshan Orogen in Central China. Progress of Natural Science 13 (12), 1238–1246.

Klepeis, K.A., Clarke, G.L., Gehrels, G., Vervoort, J., 2004. Processes controlling vertical coupling and decoupling between the upper and lower crust of orogens: results from Fiordland, New Zealand. Journal of structural geology 26 (4), 765–791.

Li, R.W., Wan, Y.S., Cheng, Z.Y., Zhou, J.X., Li, S.Y., Jin, F.Q., Meng, Q.R., Li, Z., Jiang, M.S., 2005. Provenance of Jurassic sediments in the Hefei Basin, east-central China and the contribution of high-pressure and ultrahigh-pressure metamorphic rocks from the Dabie Shan. Earth and Planetary Science Letters 231, 279–294.

Li, S.G., Jagoutz, E., Chen, Y.Z., Li, Q.L., 2000. Sm-Nd and Rb-Sr isotopic chronology and cooling history of ultrahigh pressure metamorphic rocks and their country rocks at Shuanghe in the Dabie Mountains, Central China. Geochimica et Cosmochimica Acta 64 (6), 1077–1093.

Lin, S., Jiang, D., 2001. Using along-strike variation in strain and kinematics to define the movement direction of curved transpressional shear zones: an example from northwestern Superior Province, Manitoba. Geology 29, 767–770.

Lin, W., Enami, M., Faure, M., Schärer, U., Arnaud, N., 2007. Survival of eclogite xenolith in a Cretaceous granite intruding the Central Dabieshan migmatite gneiss dome (Eastern China) and its tectonic implications. International Journal of Earth Science 96, 707–724.

Lin, W., Faure, M., Monié, P., Schärer, U., Panis, D., 2008. Mesozoic extensional Tectonics in Eastern Asia: the South Liaodong Peninsula metamorphic core complex (NE China). The Journal of Geology 116, 134–154.

Lin, W., Wang, Q.C., Faure, M., Arnaud, N., 2005. Tectonic evolution of the Dabieshan orogen: in the view from polyphase deformation of the Beihuaiyang metamorphic zone. Science in China (Series D) 48 (7), 886–899.

Liu, J.L., Davis, G.A., Lin, Z.Y., Wu, F.Y., 2005a. The Liaonan metamorphic core complex, Southeastern Liaoning Province, North China: a likely contributor to Cretaceous rotation of Eastern Liaoning, Korea and contiguous areas. Tectonophysics 407, 65–80.

Liu, M., 2001. Cenozoic extension and magmatism in the North American Cordillera: the role of gravitational collapse. Tectonophysics 342 (3–4), 407–433.

Liu, Y.C., Li, S.G., Xu, S.T., 2007. Zircon SHRIMP U-Pb dating for gneisses in northern Dabie high T/P metamorphic zone, central China: implications for decoupling within subducted continental crust. Lithos 96, 170–185.

Liu, Y.C., Li, S.G., Xu, S.T., Jahn, B.M., Zheng, Y.F., Zhang, Z.Q., Jiang, L.L., Chen, G.B., Wu, W.P., 2005b. Geochemistry and geochronology of eclogites from the northern Dabie Mountains, central China. Journal of Asian Earth Sciences 25, 431–443.

Ludwig, K.R., 2004. User's Manual for Isoplot 3.14: a Geochronological Toolkit for Microsoft Excel. Berkeley Geochronology Center Special Publication, pp. 1–70.

Ma, C.Q., Yang, K.G., Ming, H.L., Lin, G.C., 2004. The timing of tectonic transition from compression to extension in Dabieshan: evidence from Mesozoic granites. Science in China (Series D) 47 (5), 453–462.

Malaspina, N., Hermann, J., Scambelluri, M., Compagnoni, R., 2006. Multistage metasomatism in ultrahigh-pressure mafic rocks from the North Dabie Complex (China). Lithos 90, 19–42.

Maruyama, S., Liou, J.G., Zhang, R., 1994. Tectonic evolution of the ultrahigh-pressure (UHP) and high-pressure (HP) metamorphic belts from central China. The Island Arc 3 (3), 112–121.

Meissner, R., Mooney, W., 1998. Weakness of the lower continental crust: a condition for delamination, uplift, and escape. Tectonophysics 296, 47–60.

Okay, A.I., 1993. Petrology of a diamond and coesite-bearing metamorphic terrene: Dabieshan, China. European Journal of Mineralogy 5, 659–673.

Okay, A.I., Xu, S.T., Sengör, A.M., 1989. Coesite from the Dabie Shan eclogites, central China. European Journal of Mineralogy 1, 595–598.

Pryer, L.L., 1993. Microstructures in feldspars from a major crustal thrust zone: the Grenville Front, Ontario, Canada. Journal of Structural Geology 15, 21–36.

Ratschbacher, L., Hacker, B.R., Webb, L.E., McWilliams, M., Ireland, T., Dong, S., Calvert, A., Chateigner, D., Wenk, H.R., 2000. Exhumation of the ultrahigh-pressure continental crust in east central China: Cretaceous and Cenozoic unroofing and the Tan-Lu fault zone. Journal of Geophysical Research 105 (B6), 13303–13338.

Reddy, S.M., Potts, G.J., 1999. Constraining absolute deformation ages: the relationship between deformation mechanisms and isotope systematics. Journal of Structural Geology 21, 1255–1265.

Rey, P., Vanderhaeghe, O., Teyssier, C., 2001. Gravitational collapse of the continental crust: definition, regimes and modes. Tectonophysics 342, 435–449.

Rowley, D.B., Xue, F., Tucker, R.D., Peng, Z.X., Baker, J., Davis, A., 1997. Ages of ultrahigh pressure metamorphism and protolith orthogneisses from the eastern Dabie Shan: U/Pb zircon geochronology. Earth and Planetary Science Letters 151, 191–203.

Stipp, M., Stünitz, H., Heilbronner, R., Schmid, S.M., 2002. The eastern Tonale fault zone: a 'natural laboratory' for crystal plastic deformation of quartz over a temperature range from 250 to 700 °C. Journal of Structural Geology 24, 1861–1884.

Suo, S.T., Zhong, Z.Q., You, Z.D., 2000. The extension deformation during post ultrahigh-pressure metamorphism and exhumation process of UHP metamorphic rock on Dabie block. Science in China (Series D) 30 (1), 9–17.

Suo, S.T., Zhong, Z.Q., You, Z.D., 2001. Extensional tectonic framework of the Dabie-Sulu UHP-HP metamorphic belt, central China, and its geodynamical significance. Acta Geologica Sinica 75 (1), 14–24.

Tullis, J., Yund, R.A., 1991. Diffusion creep in feldspar aggregates: experimental evidence. Journal of Structural Geology 13, 987–1000.

Vanderhaeghe, O., Teyssier, C., 2001. Partial melting and flow of orogens. Tectonophysics 342, 451–472.

Wang, C.Y., Zeng, R.S., Mooney, W.D., Hacker, B.R., 2000. A crustal model of the ultrahigh-pressure Dabie Shan orogenic belt, China, derived from deep seismic refraction profiling. Journal of Geophysical Research 105 (B5), 10857–10869.

Wang, E., Meng, Q.R., Burchfiel, B.C., 2003. Mesozoic large-scale lateral extrusion, rotation, and uplift of the Tongbai-Dabie Shan belt in east China. Geology 31 (4), 307–310.

Wang, Q., Wyman, D.A., Xu, J.F., Jian, P., Zhao, Z.H., Li, C.F., Xu, W., Ma, J.L., He, B., 2007. Early Cretaceous adakitic granites in the Northern Dabie complex, central China: implications for partial melting and delamination of thickened lower crust. Geochimica et Cosmochimica Acta 71, 2609–2636.

Wang, X., Liou, J., Mao, H., 1989. Coesite-bearing eclogite from the Dabie Mountains in central China. Geology 17, 1085–1088.

Wang, X.M., Zhang, R.Y., Liou, J.G., 1995. UHPM terrane in east central China. In: Coleman, R., Wang, X. (Eds.), Ultrahigh Pressure Metamorphism. Cambridge University Press, pp. 356–390.

Williams, P.F., Jiang, D.Z., 2005. An investigation of lower crustal deformation: evidence for channel flow and its implications for tectonics and structural studies. Journal of Structural Geology 27, 1486–1504.

Wu, F.Y., Lin, J.Q., Wilde, S.A., Zhang, X.O., Yang, J.H., 2005. Nature and significance of the Early Cretaceous giant igneous event in eastern China. Earth and Planetary Science Letters 233, 103–119.

Wu, Y.B., Zheng, Y.F., Zhang, S.B., Zhao, Z.F., Wu, F.Y., Liu, X.M., 2007. Zircon U–Pb ages and Hf isotope compositions of migmatite from the North Dabie terrane in China: constraints on partial melting. Journal of Metamorphic Geology 25, 991–1009.

Xie, Z., Zheng, Y.F., Zhao, Z.F., Wu, Y.B., Wang, Z.R., Chen, J.F., Liu, X.M., Wu, F.Y., 2006. Mineral isotope evidence for the contemporaneous process of Mesozoic granite emplacement and gneiss metamorphism in the Dabie orogen. Chemical Geology 231, 214–235.

Xu, H.J., Ma, C.Q., Ye, K., 2007. Early cretaceous granitoids and their implications for the collapse of the Dabie orogen, eastern China: SHRIMP zircon U–Pb dating and geochemistry. Chemical Geology 240, 238–259.

Xu, S.T., Liu, Y.C., Chen, G.B., Roberto, C., Franco, R., He, M.C., Liu, H.F., 2003. New finding of microdiamonds in eclogites from Dabie-Sulu region in central-eastern China. Chinese Science Bulletin 48 (10), 988–994.

Xu, S.T., Okay, A.I., Sengör, A.M.C., Su, W., Liu, Y., Jiang, L., 1992. Diamond from Dabie Shan metamorphic rocks and its implication for tectonic setting. Science 256, 80–82.

Xu, Y.G., Huang, X.L., Ma, J.L., Wang, Y.B., Iizuka, Y., Xu, J.F., Wang, Q., Wu, X.Y., 2004. Crust-mantle interaction during the tectono-thermal reactivation of the North China Craton: constraints from SHRIMP zircon U-Pb chronology and geochemistry of Mesozoic plutons from western Shandong. Contributions to Mineralogy and Petrology 147, 750–767.

Yang, J.H., Wu, F.Y., Chung, S.L., Lo, C.H., Wilde, S.A., Davis, G.A., 2007. Rapid exhumation and cooling of the Liaonan metamorphic core complex: inferences from 40Ar/39Ar thermochronology and implications for Late Mesozoic extension in the eastern North China Craton. GSA Bulletin 119 (11/12), 1405–1414.

Yang, K.G., Ma, C.Q., Xu, C.H., Yang, W.R., 2000. Differential uplift between Beihuayang and Dabie orogenic belt. Science in China (Series D) 43 (2), 193–199.

Zhai, M.G., Cong, B.L., Zhao, Z., Wang, Q.C., Wang, G., Jiang, L.L., 1995. Petrological-tectonic units in the coesite-bearing metamorphic terrain of the Dabie Mountains, central China and their geotectonic implication. Journal of SE Asian Earth Sciences 1, 1–13.

Zhang, H.F., Gao, S., Zhong, Z.Q., Zhang, B.R., Zhang, L., Hu, S.H., 2002. Geochemical and Sr–Nd–Pb isotopic compositions of Cretaceous granitoids: constraints on tectonic framework and crustal structure of the Dabieshan ultrahigh -pressure metamorphic belt, China. Chemical Geology 186, 281–299.

Zhang, H.F., Sun, M., Zhou, X.H., Ying, J.F., 2005. Geochemical constraints on the origin of Mesozoic alkaline intrusive complexes from the North China Craton and tectonic implications. Lithos 81, 297–317.

Zhang, J.J., Zheng, Y.D., Liu, S.W., 2000. Application of general shear theory to the study of formation mechanism of the metamorphic core complex: a case study of Xiaoqinling, in central China. Acta Geologica Sinica 74, 19–28.

Zhang, R.Y., Liou, J.G., Tsai, C.H., 1996. Petrogenesis of a high-temperature metamorphic terraine: a new tectonic interpretation for the north Dabie Shan, central China. Journal of Metamorphic Geology 14, 319–333.

Zhao, Z.F., Zheng, Y.F., Wei, C.S., Wu, Y.B., 2007. Post-orogenic granitoids from the Dabie orogen in China: zircon U-Pb age, element and O isotope evidence for recycling of subducted continental crust. Lithos 93, 248–272.

Zhao, Z.F., Zheng, Y.F., Wei, C.S., Wu, Y.B., Chen, F.K., Jahn, B.M., 2005. Zircon U-Pb age, element and C-O isotope geochemistry of post-collisional mafic-ultramafic rocks from the Dabie orogen in east-central China. Lithos 83, 1–28.

Zhong, Z.Q., Suo, S.T., You, Z.D., 1998. Extensional tectonic framework of post high and ultrahigh pressure metamorphism in Dabieshan, China. Earth Science 23 (3), 225–229.

Zhou, J.B., Zheng, Y.F., Li, L., Xie, Z., 2001. Accretionary wedge of the subduction of the Yangtze plate. Acta Geologica Sinica 75 (3), 338–353.

Zhu, G., Niu, M.L., Xie, C.L., Wang, Y.S., 2010a. Sinistral to normal faulting along the Tan-Lu fault zone: evidence for geodynamic switching of the east China continental margin. The Journal of Geology 118, 277–293.

Zhu, G., Wang, Y.S., Liu, G.S., Niu, M.L., Xie, C.L., Li, C.C., 2005. $^{40}Ar/^{39}Ar$ dating of strike-slip motion on the Tan-Lu fault zone, East China. Journal of structural geology 27, 1379–1398.

Zhu, G., Xie, C.L., Chen, W., Xiang, B.W., Hu, Z.Q., 2010b. Evolution of the Hongzhen metamorphic core complex: evidence for Early Cretaceous extension in the eastern Yangtze craton, eastern China. GSA Bulletin 122 (3/4), 506–516.